Meander chute cutoff at an alluvial river facilitated by gypsum sinkholes

Schwendel A. C.[1], Cooper A. H.[2]

[1] School of Humanities, York St John University, Lord Mayor's Walk, York YO31 7EX, UK, a.schwendel@yorksj.ac.uk

[2] British Geological Survey, Nottingham, UK

Abstract

Collapse sinkholes are common in areas where gypsum strata underlie rock that is incompetent to bridge the cavities created by the groundwater dissolution of gypsum. On floodplains these can be obscured due to fill by overbank deposits, and channels tend to migrate towards larger enclosed depressions. This study utilises GIS to analyse the influence exerted by small collapse sinkholes on the channel dynamics of the alluvial River Ure, UK. At Ripon Loop, a large compound meander bend, sinkhole area and channel dynamics have been tracked over > 160 years from multiple datasets, including historic maps, aerial imagery, lidar and a Structure-from-Motion photogrammetry dataset acquired for this study. This indicated two distinct populations, firstly long-lived, constant-sized sinkholes and secondly dynamically growing holes aligned with the contact of bedrock and unconsolidated materials of a buried valley at depth where artesian water saturated with sulphate enters the latter. Frequent overbank flows of the River Ure across the neck of the bend have interacted with sinkholes, e.g. by deposition of bedload in the down-valley end of the holes and localised headward incision on the opposite side due to the relatively high gradient between holes and the downstream limb. The location of holes has conditioned the incision of small shallow channels over at least seven years before cutoff occurred over several floods in 2019. Initially overbank flow traversed the neck via the chain of sinkholes before widening and deepening of the channel captured all the surface flow of the River Ure resulting in the mobilisation of more than 20,000 m^3 of sediment. Allogenic influences on fluvial systems in relation to meander dynamics are often neglected and this study is the first to link floodplain sinkholes with detailed mechanisms of a chute cutoff, hereby indicating a potential feedback to sinkhole dissolution processes.

Key words: subsidence, collapse doline, gypsum karst, gravel-bed river, photogrammetry, lidar

1. Introduction

The cycle of bend development, growth and eventually their cutoff is an inherent autogenic characteristic of meandering rivers driven by non-linear processes (Hooke, 1995; Camporeale et al., 2005; Seminara, 2006; Camporeale et al., 2008; Constantine and Dunne, 2008). Erosion of cutbanks and accumulation of sediment on the point bar drives bend migration of alluvial channels (Parker et al., 2011; Zolezzi et al., 2012). With increasing bend length, curvature grows and the bends upstream and downstream may migrate towards each other, hereby forming the neck of a meander. The abandonment of a meander bend and thus shortening of the river reach is facilitated via a breach or cutoff channel across the neck of the bend. Where the neck has been gradually eroded by migrating bends upstream and downstream, these breaches are a result of intersection, hereby forming a neck cutoff which is a typical feature of low-gradient rivers with stable banks and high suspended sediment load (Lewis and Lewin, 1983; Tal and Paola, 2010; Constantine et al., 2014; Ahmed et al., 2019). In contrast, cutoffs via longer channels across the meander neck are termed chute cutoffs and more common in higher gradient gravel-bed rivers (Lewis and Lewin, 1983) or sand-bed rivers with limited suspended sediment load (Howard, 2009; Grenfell et al., 2012; van Dijk et al., 2013).

While neck cutoffs have been studied extensively (e.g. Gay et al., 1998; Hooke, 1995; Hooke, 2007; Camporeale et al., 2008; Constantine and Dunne, 2008; Schwendel et al., 2015) and have been successfully modelled physically (Han and Endreny, 2014) and mathematically (e.g. Howard and Knutson, 1984; Johannesson and Parker, 1989; Stolum, 1996; Sun et al., 1996; Lancaster and Bras, 2002; Camporeale et al., 2005; Frascati and Lanzoni, 2010; Motta et al., 2012), empirical studies of chute cutoffs are rarer due to the lower predictability and more complex modelling (Seminara, 2006; Frascati and Lanzoni, 2010). Nevertheless, chute cutoffs have been included in numerical meander models (Howard, 1996; Viero et al., 2018) and in physical models they have limited sinuosity in single thread meandering channels (Smith, 1998; Peakall et al., 2007; Braudrick et al., 2009; Tal and Paola, 2010; van Dijk et al., 2013). These models and empirical studies have attributed planform bend geometry, direction and inertia of flow, near-bank flow velocity, floodplain topography, vegetation and point bar

sedimentology as spatial controls and excess bankfull discharge as temporal control on the formation of chute channels (Howard, 1996; Constantine et al., 2010; Luchi et al., 2011; Micheli and Larsen, 2011; Viero et al., 2018).

1.1 Chute incision process

Chute channels can form across the active point bar (partial cutoff) or at any point across the neck (Lewis and Lewin, 1983; Fares and Herbertson, 1990; Micheli and Larsen, 2011). An initial probe channel may incise and, driven by slope advantage, widen until it captures a considerable proportion of the entire flow, resulting in either persistent bifurcations or eventual abandonment of the longer channel reach to form a chute cutoff. The process of incision of such a cutoff channel has been attributed to a range of processes including scour from overbank flows (Johnson and Paynter, 1967; Bridge et al., 1986; Hooke, 1995; Gay et al., 1998; Peakall et al., 2007; Constantine et al., 2010; Grenfell et al., 2012) and seepage across the neck (Johnson and Paynter, 1967; Han and Endreny, 2014). In the former case flow across the point bar can be promoted by aggradation of bars just upstream of the apex of a rapidly extending bend (Peakall et al., 2007), deposition of unit bars in the upstream limb (Johnson and Paynter, 1967; Ashmore, 1991; Thompson, 2003; Eekhout and Hoitink, 2015;), flow obstruction by ice (Keller and Swanson, 1979; Gay et al., 1998) or woody debris (Keller and Swanson, 1979), or changes in the angle of approach of the flow after cutoffs in upstream bends (Bridge et al., 1986; Peakall et al., 2007; Schwendel et al., 2015). Three principal mechanisms of how overbank flow will form a chute channel have been recognised: 1, headward incision from the downstream limb; 2, incision and downstream extension of an embayment from the upstream limb; 3, the enlargement of existing topographic depressions. Headward incision is promoted by high flow velocities where the overbank flow rejoins the downstream channel due to the elevation difference between floodplain and channel. Constantine et al. (2010) suggest that rill and gully formation might be responsible for initiating these headcuts and Gay et al. (1998) observed the concentration of flow from initially several gullies into a single headcut. This mechanism has been reported from several coarse-bed rivers (Thompson, 2003; Zinger et al., 2011). The second mechanism, the extension of an embayment formed by bank erosion from the upstream channel across the neck has been observed in a range of settings (Constantine et al., 2010; Eekhout and Hoitink, 2015; Harrison et al., 2015). The location for initial embayment is typically just downstream of the apex of the bend immediately upstream of the cutoff bend where boundary shear stress

during overbank flows is high (McGowen and Garner, 1970; Constantine et al., 2010; Harrison et al., 2015). The success of this mechanism is conditioned by floodplain vegetation structure and overbank deposition of suspended sediment (Constantine et al., 2010). The third mechanism involves routing of overbank flow along preferred corridors across the point bar. These corridors for channelisation of flow can be characterised by their vegetation structure or their low topography. Chute incision can be enhanced in areas of sparse vegetation where roughness is low and roothold is limited (Micheli and Larsen, 2011; Grenfell et al., 2012). In addition, areas of low topography, particularly when aligned across the point bar such as abandoned channels or swales at rivers with scroll bars, provide efficient proto-channels for chutes (Fisk, 1947; Bridge et al., 1986; Mertes et al., 1996; Grenfell et al., 2012; Schwendel et al., 2018; Viero et al., 2018).

1.2 Allogenic influences on chute cutoff and channel dynamics

Many processes associated with meandering can be attributed to autogenic, self-organised behaviour (Hooke, 2007). Abandoned channels, ridge-swale topography on point bars and variability in the erodibility of floodplain sediments can be considered autogenic features of the fluvial system. Allogenic influences on channel routing and in particular the development of chute cutoffs are less well researched. Terraces, valley walls and bedrock have been recognised as constraints to meander migration and channel dynamics in alluvial settings (Hooke, 1995; Tooth et al., 2002; Hooke, 2007; Dean and Schmidt, 2013; Schwendel et al., 2015) but the influence of karstic subsidence at the channel-scale has gained less attention. On a landscape scale the alignment of valleys and basins with zones of dissolution-induced subsidence has been examined (Gustavson, 1986; Benito et al., 2000) and at larger scales syn-sedimentary subsidence of floodplains and terraces due to dissolution of underlying evaporites has been researched, particularly in the Tertiary Ebro basin (Gutiérrez, 1996; Benito et al., 1998; Guerrero and Lucha, 2008). On floodplains, subsidence features can range from large closed depressions to small collapse sinkholes (Gutiérrez et al., 2007; Galve et al., 2009) and the latter are often aligned with the valley edge where groundwater circulation enhances dissolution rates (Benito et al., 1998; Cooper, 1998). Fluvial systems tend to accommodate subsidence by aggradation in order to maintain an equilibrium long profile (Gutiérrez, 1996; Benito et al., 1998; Guerrero and Lucha, 2008;). Diffluent flow into deep gravel deposits can lead to locally convex long-profiles due to loss of flow competence (Benito et al., 1998) and differential subsidence along a valley

can invoke transition between braiding and meandering planform (Guerrero and Lucha, 2008). In addition to the thickness of alluvial deposits, dissolution-induced subsidence has been observed to cause decrease in sediment calibre (e.g. higher proportion of floodplain sediments; Guerrero and Lucha, 2008), local ponded areas and swamps (Benito et al., 2000; 1998), changes to size and geometry of the channel (Gutiérrez, 1996) and increase in sinuosity (Benito et al., 1998). Channel migration towards large closed depressions on the floodplain (Gutiérrez, 1996; Benito et al., 1998; Doğan, 2005) and a general shift towards evaporite outcrops in the often asymmetric valleys has been observed (Gutiérrez, 1996; Gutiérrez et al., 2007; Guerrero and Lucha, 2008). In the latter case, the valleys in the Ebro basin are often dominated by a rapidly retreating evaporite escarpment on one valley side, which is more erodible than the floodplain deposits and thus attracts channel migration. Collapse sinkholes can be frequent on floodplains (Gustavson et al., 1982; Cooper, 1986; 1989; Gutiérrez et al., 2007; Castañeda et al., 2009; Galve et al., 2009) but they are often filled quickly anthropogenically or by floodplain deposits (Cooper, 1986; Gutiérrez, 1996; Gutiérrez et al., 2007) and may provide detailed sedimentological flood records (Gutiérrez et al., 2017). While some studies show sedimentological evidence of contact between an active river channel and sinkholes (Gutiérrez, 1996), associated processes have not been recorded to date. Equally, the influence of small sinkholes on fluvial processes such as meander cutoff are unexplored. This study provides the first analysis of the interaction between contemporary chute cutoff processes and sinkhole activity on the floodplain. For the example of Ripon Loop on the River Ure, the history of floodplain sinkholes, facilitation of overbank flows and channel shortening, and the resulting topographic changes are examined and discussed.

2. Site and setting

The River Ure in North Yorkshire is a main tributary of the River Ouse which drains the Yorkshire Dales (Pennines) and the Vale of York and flows via the Humber estuary into the North Sea. The River Ure's catchment at Ripon covers an area of approximately 634 km^2 (Sear et al., 2000) which is dominated by Carboniferous sandstones and limestones partially covered by superficial glacial deposits and peat. The highest elevation in the catchment is 716 m while Ripon has an elevation of 19 m asl (Sear et al., 2000). Catchment landcover is dominated by grassland and mean annual catchment rainfall is approximately 1120 mm (calculated for Westwick gauge, 6 km downstream from Ripon; NRFA, 2021a). Mean annual discharge at Ripon can be estimated as 20.5 $m^3 s^{-1}$ by

comparing data from Westwick gauge and a gauge on the main tributary between Ripon and Westwick (NRFA, 2021b).

Ripon Loop is a meander bend of the River Ure situated two kilometres NNE of Ripon, North Yorkshire, UK (Fig. 1). The River Ure flows between West Tanfield and Ripon in a NNW-SSE direction, largely aligned with a buried valley that extends from North Stainley past Ripon to Newby Hall where it turns east into the Vale of York as indicated by rockhead elevation (British Geological Survey, 1987a; 1987b; 1992a; 1992b). The buried valley is approximately 900 m wide at Ripon Loop but narrows considerably to about 180 m past Ripon before widening again to the south. The valley has a basal elevation of about -10m below OD and is largely filled with up to 30 m (more in places where subsidence has occurred) of glacial and glacio-fluvial sands and gravel as well as Holocene alluvial deposits (Morigi and James, 1984; Powell et al., 1992; Cooper and Burgess, 1993). The geological maps show that the valley intersects late Permian and early-Triassic sedimentary rocks (Powell et al., 1992; Cooper and Burgess, 1993). This geological sequence is shown in Figure 1 and is notable for including thick units of highly soluble gypsum (James et al., 1981) associated with soft mudstones in the Edlington Formation (up to 40 m of gypsum) and Roxby Formation (up to 10 m of gypsum). These soluble and easily eroded formations are sandwiched between the aquifers of the Cadeby Formation dolostones, Brotherton Formation limestones and the Sherwood Sandstone Group sandstones. After the initial glacial incision of the buried valley, it has continued to evolve becoming wider and deeper due to groundwater induced gypsum dissolution that causes a sinkhole hazard in the Ripon area and along the buried valley (Cooper, 1986; Patterson et al., 1995; Cooper et al., 2013; Cooper, 2020). Gypsum dissolution continues to occur on both sides and beneath the valley and this is attested by subsidence, but also by sulphate rich springs (Cooper et al., 2013) and spring-related tufa-cemented gravels such as those proved in borehole SE37SW/103 [3165,7366] on the southern part of the Ripon Loop and SE37SW/106 [3155,7268] near Ripon (Morigi and James, 1984).

Except where it is cemented with tufa, the River Ure has incised the present alluvial tract into relatively unconsolidated superficial deposits of the buried valley with the floodplain being in places constraint by bedrock outcrops (James et al., 1981; Cooper, 2020) and bounded by numerous fluvial and glacio-fluvial terraces (Morigi and James, 1984; e.g. in Fig. 2 North of the 1850s channel). This configuration has promoted sedimentation of a wide alluvial body that reaches 900 m in width at Ripon Loop (Sear et al., 2000). At Ripon Loop considerable meander migration dynamics are evidenced from exposures in cutbanks, the outline of parish boundaries

originally situated in mid-channel and mapped river courses over the past 170 years (Fig. 2). Overbank flows at Ripon Loop start if a level of 0.93 m is equalled or exceeded at Ripon Ure Bank stage monitoring station which occurs at 4.75% of time during a 22.3 year stage record (Environment Agency, unpublished data). These data reveal that overbank flows happen on average every 13.7 days with a mean duration of 15.3 h. The river bed at Ripon Loop consists of gravels and cobbles.

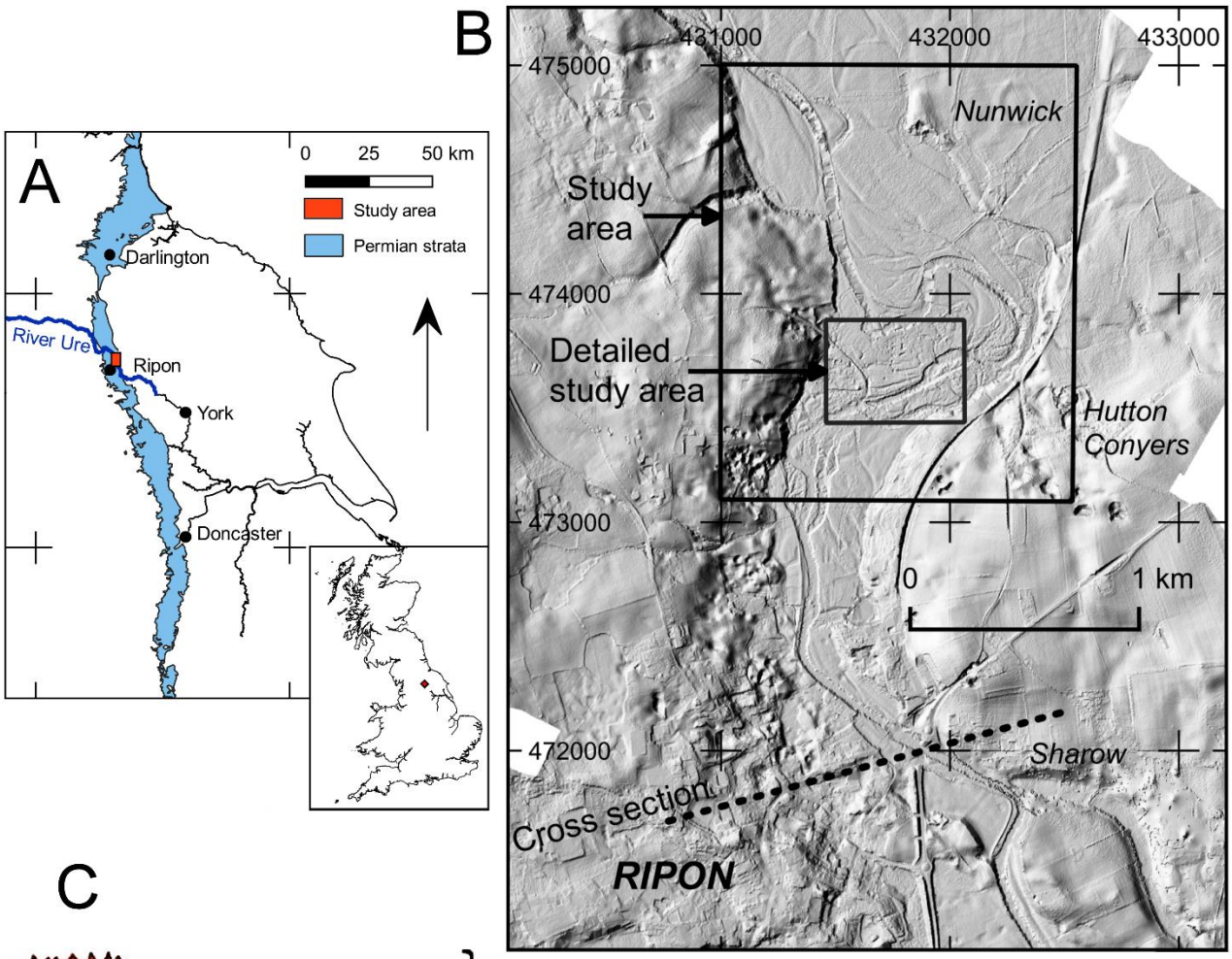
A
0 25 50 km
Study area
Permian strata
Darlington
River Ure
Ripon
York
Doncaster
B
431000
432000
433000
475000
474000
473000
472000
Nunwick
Study area
Detailed study area
Hutton Conyers
0 1 km
Sharow
Cross section
RIPON

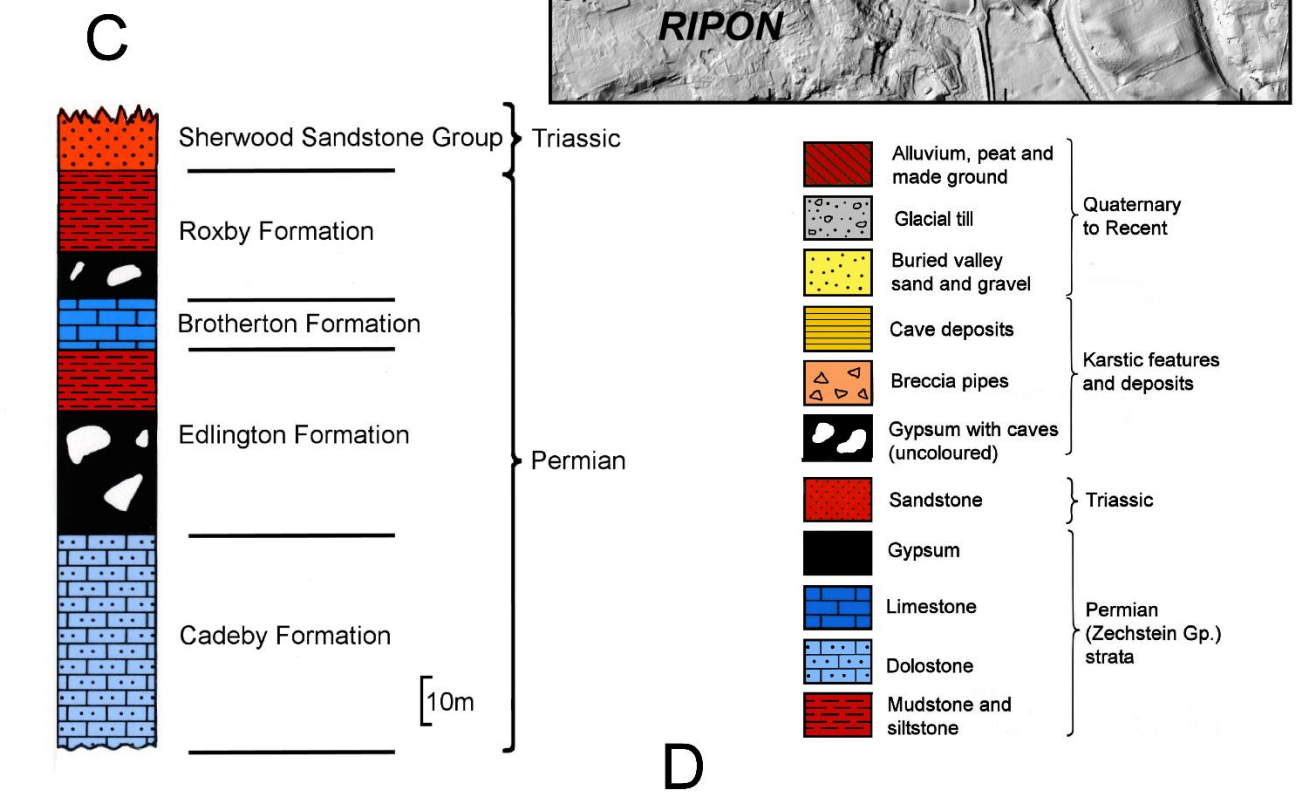
C
Sherwood Sandstone Group
Triassic
Roxby Formation
Brotherton Formation
Edlington Formation
Cadeby Formation
Permian
10m
Alluvium, peat and made ground
Glacial till
Buried valley sand and gravel
Quaternary to Recent
Cave deposits
Breccia pipes
Gypsum with caves (uncoloured)
Karstic features and deposits
Sandstone
Triassic
Gypsum
Limestone
Dolostone
Mudstone and siltstone
Permian (Zechstein Gp.) strata

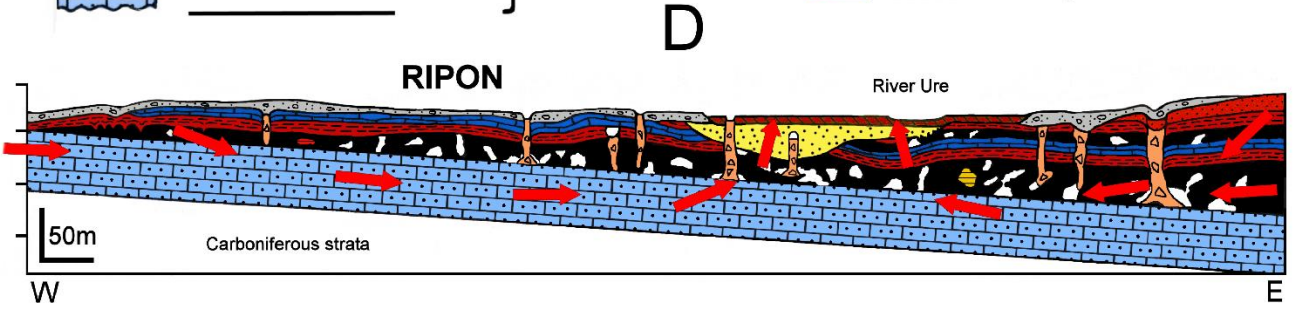
D
RIPON
River Ure
50m
Carboniferous strata
W
E

Figure 1. Study site: A) The River Ure/ Ouse and Ripon within Northern England and distribution of gypsiferous strata, B) Locations of study site and cross-section overlaid on a shaded relief map based on the 2001 Environment Agency 2m resolution Lidar. C) generalised vertical section at Ripon and D) cross-section through the Ripon area showing gypsum strata and the buried valley of the Proto-Ure. (Modified with the permission of the British Geological Survey from Cooper (2020), Fig. 16.2) Geological map 625K open data - Contains British Geological Survey materials ©BGS UKRI 2021; rivers and coast- Contains OS data © Crown copyright 2021; Lidar - Contains Environment Agency information © Environment Agency and/or database right 2021.

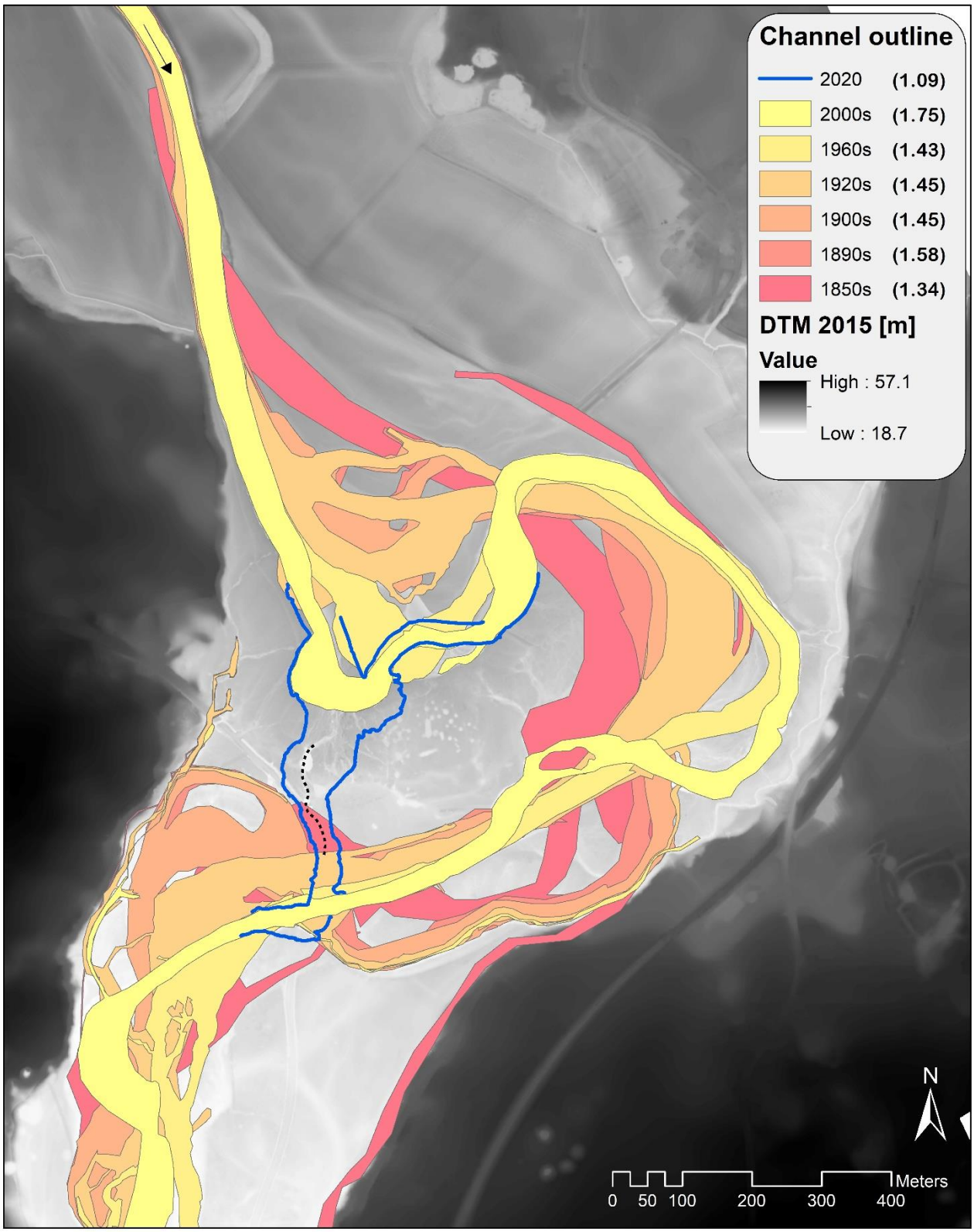

Figure 2. Channel migration at Ripon Loop between the 1850s and 2020. Respective sinuosity is given in brackets in the legend. Flow is from North to South. The initial chute channel in 2019 follows the line of sinkholes along the dotted line and also visible on the background 2015 lidar Digital Terrain Model England

(Open Government Licence, contains Environment Agency information © Environment Agency and/or database right 2021) and later widened to the extent shown by the 2020 outline.

Over at least the last 170 years Ripon Loop has constituted a clockwise compound loop with numerous small bifurcations and increasing sinuosity from 1.35 in the 1850s to 1.45 in the 1900s (Fig. 1, see also Sear et al. (2000)). In the early 20th century several small chute cutoffs have occurred on small bends within the loop and temporarily lowered sinuosity. Since then, the Ripon Loop compound bend has experienced down-valley translation and anti-clockwise rotation (Fig. 2) reaching a sinuosity of 1.80 in 2019. Following several floods in autumn 2019 a chute cutoff occurred in December (Fig. 2) lowering the sinuosity to 1.09 (Fig. 1) which is analysed in this paper.

There is little documentation or evidence for anthropogenic channel modification at Ripon Loop (Sear et al., 2000), aside from very localised bank protection in the form of several metres of rubble emplacement along a cutbank in the North, and the foundations of bridge heads of a former vehicular bridge in the South. The area enclosed by Ripon Loop and the surrounding land have a history of agricultural land use as pasture and as military training grounds throughout the 20th century. As a result of the latter, trenches, explosion craters and a concrete track are present (NYCC, 2021). Since 2001 the area within Ripon Loop has been a nature reserve which includes semi-natural woodlands, grassland and scrub.

3. Methods

The reconstruction of meander bend migration dynamics has been carried out in ArcGIS (version 10.5.1, ESRI, Redlands, USA) using channel outlines digitised from historic Ordnance Survey maps (EDINA Historic Digimap Service, Edinburgh, UK). The presence of sinkholes on the Ure floodplain was identified by the British Geological Survey mapping (Cooper, 1986) and elaborated in 1986 by airborne remote sensing (Cooper, 1989). Further revisions to the geological mapping and sinkhole distribution were made by Cooper for the Ripon subsidence study (British Geological Survey, 1996; Thompson et al., 1996). The present investigation of the sinkhole history of the area was undertaken using QGIS (version 3.10) and the datasets listed in Table 1. The sinkholes in the study

area were identified and digitised for each time interval. It must be noted that as time has progressed more detailed information and datasets have become available going from maps to aerial photographs then to lidar. The much greater amount of information in the most recent datasets introduces a bias and many features that can be seen on imagery and lidar would not have been recorded in the map data that tends to show only the larger features and ponds. For the map data the sinkholes on the loop area were all sites shown as ponds. Because many of the map generations record “major changes only” it is not clear whether items such as ponds were updated in every version, though the changes in river course were. The Ordnance Survey maps from 1909 to 1957 had the same ponds, but earlier and later maps are different.

Table 1. Datasets, dates and sources of information used to identify sinkholes in the study area.

Year	Data type	Source
c.05/2019	Colour aerial photography	Bing/Ordnance Survey WMS server
05/2018	Colour aerial photography	Google Maps WMS server
17/07/2017	Colour aerial photography	Getmapping Plc/EDINA
2015	Lidar 50 cm resolution Colour aerial photography	Environment Agency ESRI WMS map server
19/06/2011	Colour aerial photography	Getmapping Plc/EDINA
2009	Lidar 1 m resolution	Environment Agency
12/2002	Colour aerial photography	Google Earth
2001	Lidar 2 m resolution	Environment Agency

13/05/1986 16/05/1986 11/09/1986	B&W aerial photography and airborne multispectral scanning 1.5-2 m resolution	NERC ARSF data from CEDA, originally flown for co-author (described in Cooper (1989)) – Aerial photography 13/05/1986
1968	Map 1:2500 scale	Ordnance Survey, Landmark Information Gp. Ltd/ EDINA
1957	Map 1:10,560 scale	Ordnance Survey, Landmark Information Gp. Ltd/ EDINA
1938	Map 1:10,560 scale	Ordnance Survey, Landmark Information Gp. Ltd/ EDINA
1929	Map 1:2500 scale	Ordnance Survey, Landmark Information Gp. Ltd/ EDINA
1909	Map 1:2500 scale	Ordnance Survey, Landmark Information Gp. Ltd/ EDINA
1892	Map 1:2500 scale	Ordnance Survey, Landmark Information Gp. Ltd/ EDINA
1856	Map 1:10,560 scale	Ordnance Survey, Landmark Information Gp. Ltd/ EDINA

Detailed information was digitised from the aerial photography, but tree cover meant that in some places the sinkhole features could not be seen. The most recent aerial photography used was obtained from the Bing and Google WMS servers directly into QGIS using the add XYZ tiles functionality. The Esri server also held photography in the world imagery layer that complemented the EA 2015 lidar. The 2002 aerial photography was digitised in Google Earth and saved as a KML file which was imported into QGIS. The 1986 NERC ARSF (Airborne Research & Survey Facility) black and white photography was warped into place with multiple control points. The NERC ARSF airborne multispectral scanning data originally obtained for Cooper (1989) was imported into QGIS and warped using multiple correlation points and thin plate spline distortion with cubic spline interpolation. This allowed the data to be reasonably georeferenced, but not all the scan line “wobble” of such ancient data was removed. The eleven wavebands of data were processed in QGIS using the raster layers display functionality. Effectively the data was reprocessed in a similar manner to the original processing done by Cooper (1989), but with the added advantage that it could be utilised in GIS, a tool that had not been invented then. Used in conjunction with the aerial photography, vegetation changes, and water-filled sinkhole areas surrounded by trees, could be delineated with this data with high confidence.

The most complete information was obtained from the Environment Agency (EA) DTM lidar datasets. These allowed even small and shallow sinkholes to be identified and areas of former military earthworks. Various visualisation enhancements were undertaken to help with the digitisation of the information. Much of the site is of a fairly flat nature, consequently, colour ramping over a restricted elevation from river level to river terrace level proved effective in showing enclosed depressions, especially when combined with hillshade. Red relief image maps combined with topographic openness (Doneus, 2013; Daxter, 2020; Gökkaya et al., 2021) gave good renditions of enclosed hollows; combining these with hillshade provided the best visual information (Fig. 3). A second approach was also used to automatically allow the extraction of depression polygons. This utilised the technique of raster differencing between the filled DTM minus the original one (Doctor and Young, 2013). The original DTM was filled using the QGIS SAGA Terrain Analysis – Hydrogeology plugin "Fill sinks (Wang and Liu xxl)" written for large datasets. Using raster calculator, the original DTM was then subtracted from this filled dataset to leave just the depressions (Fig. 4). This was filtered to exclude anything shallower than 0.25 m removing much of the noise and keeping well within the elevation accuracy of the dataset. The resulting raster delineated the depressions on the flat ground well but was less successful on sloping ground. Vector data was extracted automatically from this raster information, but it was found that manual digitisation gave the most accurate results.

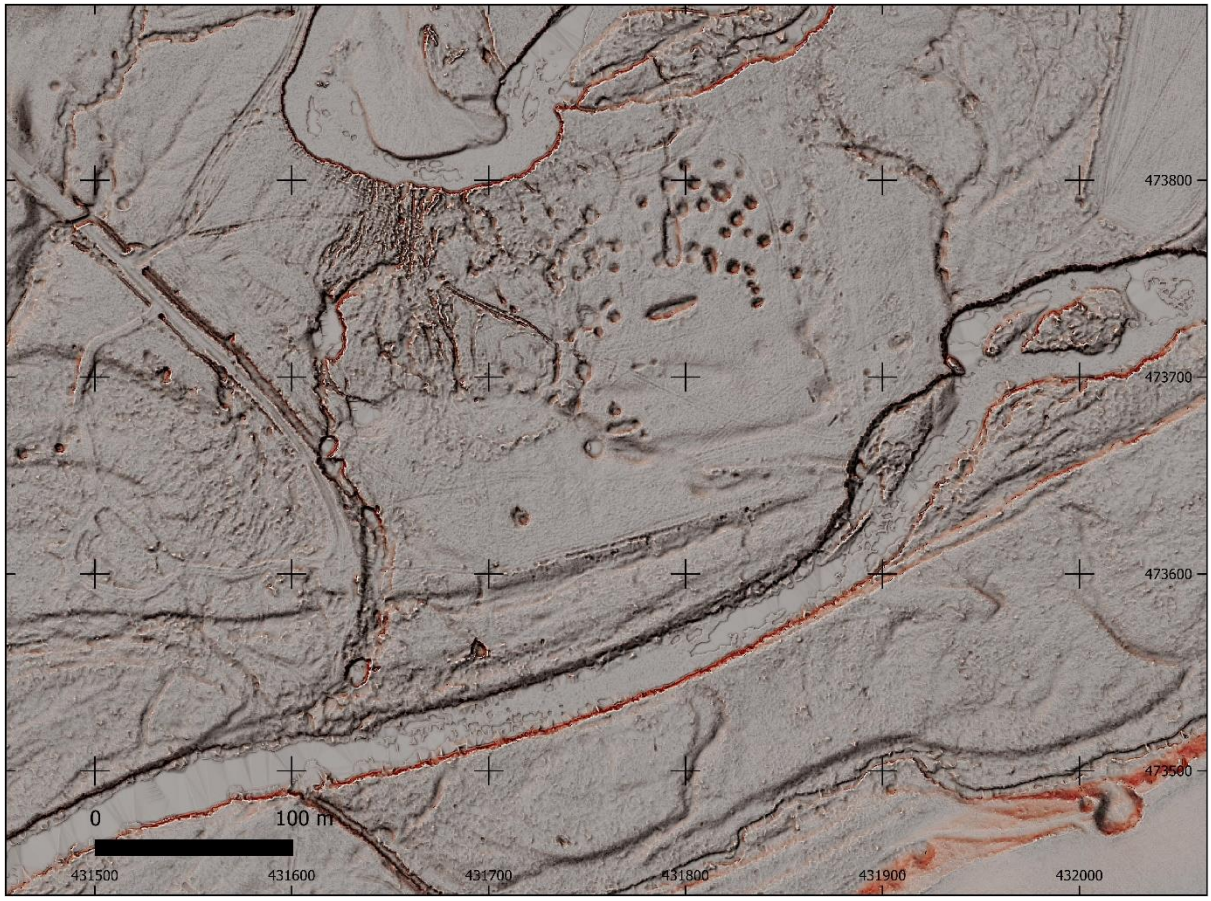

Figure 3. Lidar data (Environment Agency 2015, 50 cm) processed in QGIS using the multiply function for the overlay of slope positive and negative openness over hillshade - Contains Environment Agency information © Environment Agency and/or database right 2021.

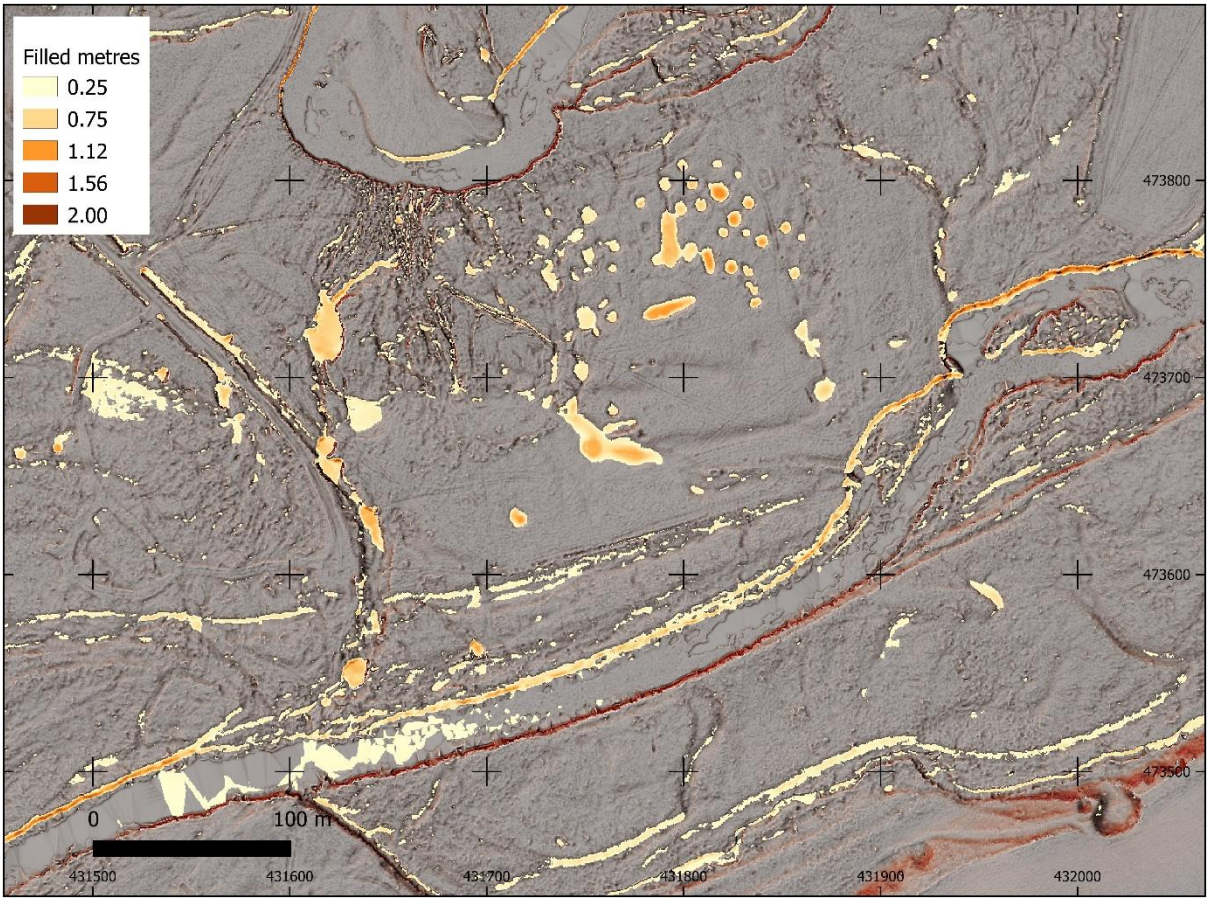

Figure 4. Filled depressions shown on lidar data (Environment Agency 2015, 50 cm) processed in QGIS using the multiply function for the overlay of slope positive and negative openness over hillshade - Contains Environment Agency information © Environment Agency and/or database right 2021.

The topographic effect of the cutoff was investigated based on differencing of two additional datasets. The first of these is the 2015 Environment Agency lidar point cloud (SE 3173, SE3174 and SE3273; 0.5 m resolution, EDINA LIDAR Digimap Service, Edinburgh, UK) using only points classified as ground and low vegetation. This was modified to account for substantial bank erosion on the upstream bend between 2015 and 2019 with the bankline from October 2019 as identified and digitised from aerial and terrestrial photographs with an uncertainty of approximately +-0.5 m. The eroded volume was removed, and the water surface extended from upstream in CloudCompare (version 2.10, 2020). The second dataset was derived from aerial imagery acquired in early March 2020 from a Phantom 4 Pro UAV (DJI, Shenzhen, PD China) flown at a height of approximately 50 m above ground. The in-built 20 Mpixel camera FC6310S has an 8.8 mm focal length and was used in mechanical shutter mode. The 2.54 cm sensor allows for 5472*3078 pixel images of 1.34 cm ground resolution which were

saved in JPEG format. The survey was carried out on a software-designed grid to allow for 80% and 65% image overlap in forward and lateral direction respectively. The vertical gridded images were supplemented by oblique images taken at lower heights and different azimuths in order to cover vertical banks and to counter systematic error introduced by inaccurate representation of radial lens distortion in the camera model (James and Robson, 2014).

Ground control was provided by 36 ground control points (GCPs) marked by coloured foam mats which were scattered across the study area (Fig. 5). Their position was measured in OSGB36 (EPSG: 27700) coordinate system using a Trimble dGNSS system (R10, Trimble Navigation Ltd., Sunnyvale, USA) at a nominal accuracy of a few centimetres. However, due to grassy and rough surfaces a general accuracy of 5 cm was estimated.

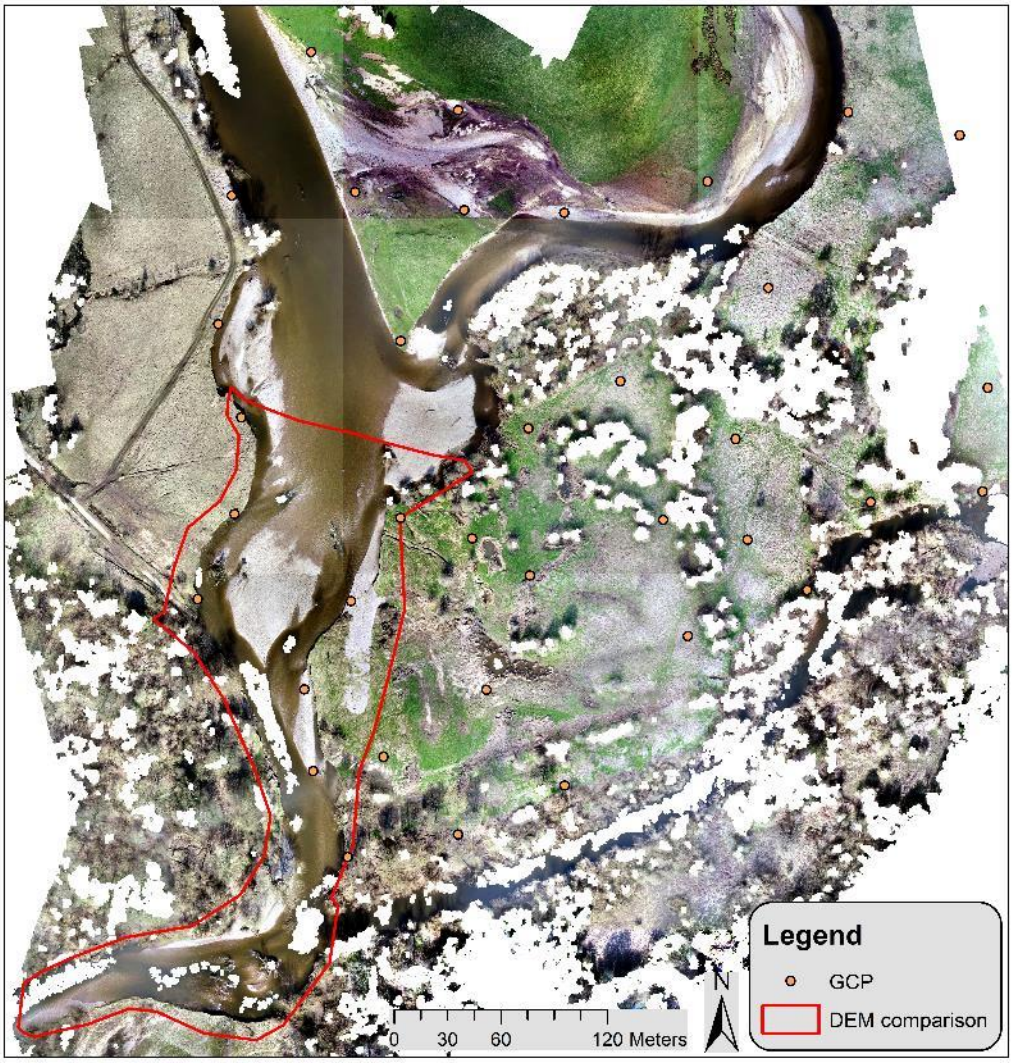

Figure 5. Study site shown as Orthophoto from March 2020 without higher vegetation or deep water. The area used for DEM comparison comprised the chute cutoff and the channel directly downstream. Ground control points (GCP) for georeferencing of the point cloud are shown.

The photogrammetric survey resulted in the acquisition of 1273 photos, covering an area of 0.292 km^2 which were processed in Agisoft Metashape (version 1.6.2, Agisoft LLC, St. Petersburg, Russian Federation). After an initial quality check and image alignment using the Scale-Invariant-Feature-Transform (SIFT) algorithm (highest accuracy, generic and reference (source) preselection, key point limit: 40000, unlimited tie points) 94% of photos were retained and a sparse point cloud of $2.8*10^6$ points was produced. The latter underwent filtering in order to remove points of insufficient projection accuracy and reconstruction uncertainty (4.4% of points), resulting in a RMS reprojection error of 0.33 pixel with every point in areas of interest projected based on the overlap of at least eight images. After application of the Multi-View Stereo (MVS) algorithm (settings: ultra high quality, moderate depth filtering), ground points were classified manually and automatically. The latter involved the application of a low pass filter (search radius 1 m, maximal variation in elevation 5 m and angle of <15° between a ground class point and a preliminary ground surface consisting of the lowest point in each search) to the dense point cloud. This was followed by further manual classification in order to exclude points representing water surface, remnants of high vegetation and other noise. Two sub-datasets were extracted from this point cloud: a) a point cloud representing surfaces that are likely to have experienced none or insignificant topographic change since 2015 due to fluvial action (stable surfaces) and b) the area of interest for comparison with the lidar point cloud (Fig. 5). The stable surfaces cloud was then co-registered in CloudCompare to the equivalent 2015 lidar cloud (ground and low vegetation classes only), including compensation for cloud-scale non-linear deviations, and the same transformation applied to the cloud covering the entire area of interest.

The point clouds representing the topography in October 2019 and March 2020 were then converted to DEMs in Surfer (version 19.2.213, Golden Software, Golden, USA) using triangulation with linear interpolation as the interpolation algorithm (Schwendel et al., 2012), with a grid spacing of 0.5 m. Blanking of areas without data (e.g. water) was conditioned based on a preliminary comparison of the two DEMs, so that where deposition was indicated above a water surface and where erosion to a 2020 water level was shown, no no-data areas were assigned. This ensured that a minimum of topographic change to and from water levels could be registered.

The assessment of error is complex in a scenario where data of various origin and accuracy is used and then processed in multiple steps which can all induce error. In this case the final DEM of difference (DoD) is

compounded by systematic and random errors arising from lidar data acquisition, various algorithms within Structure-from-Motion (SfM) photogrammetry processing, dGNSS data acquisition, co-registration of point clouds and DEM interpolation. Some of these could not be quantified or are based on small samples. The co-registration of stable parts of the two point clouds showed an RMS error of 0.31 m for a subsample of 50000 points which, given the resolution of the lidar dataset, is acceptable and mitigates for systematic errors arising from SfM processing and GCP accuracy. In order to recognise the error arising from optical acquisition of point clouds and their interpolation to a grid, and its relationship with spatial distribution of topographic variability (Heritage et al., 2009), this study follows the approach outlined in Milan et al. (2011) to derive a spatially variable level of detection for the final DoD. In brief, this requires assessment of topographic variability of both point clouds which can be expressed independently of the sample size (cloud density) as the standard deviation within a moving window with a radius of 1.5 m. Because the standard deviation becomes more stable with increasing sample size, a minimum sample size of 25 points within the moving window was applied. Plotting the residual DEM error versus topographic variability (Fig. 6 a, b) shows an increase in variability with increasing absolute error with larger errors associated with the 2019 dataset which can be explained by its much lower resolution. In order to relate the variation within residual errors to the topographic variability, the standard deviation of residual error within 100 classes of topographic variability was calculated (Fig. 6 c, d) and explored using linear regression in Scipy (Virtanen et al., 2020). The regression shows a strong linear relationship with R^2s of 0.997 and 0.832 respectively and the regression equations have thus been applied to the topographic variability grids to compute the spatially variable distribution of error for each dataset. The error propagated to the DoD is commonly calculated as the RMSE of the component standard deviation of errors σ_1 and σ_2 (Brasington et al., 2000; 2003; Lane et al., 2003; Milan et al., 2007) and is termed the level of detection (LoD):

$$LoD = t\sqrt{(\sigma_1)^2 + (\sigma_2)^2} \qquad (1)$$

with *t* being the critical t-value at the chosen confidence level here set at a value of 1.96 (2σ), in which case the confidence limit is equal to 95%. In order to assess the spatial distribution of topographic change as a result of the cutoff, the 2020 and 2019 DEMs were subtracted with the LoD applied to the resulting DoD. Erosion and deposition were quantified respectively as the negative and positive volume of the LoD-corrected DoD.

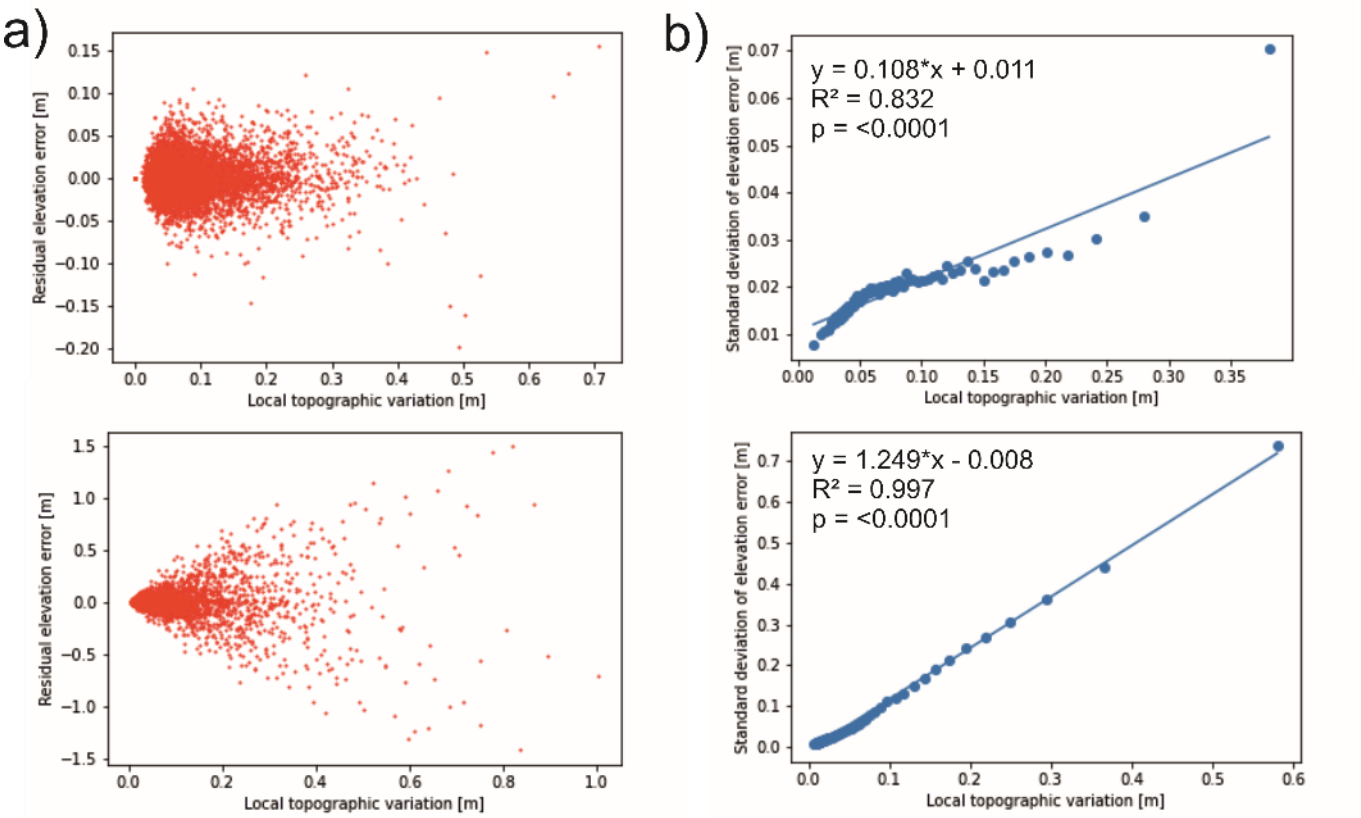

Figure 6. Variation in residual elevation error of the DEMs (top panels 2019, bottom panels 2020) with topographic variability: a) residual error plotted against topographic variability, assessed as the standard deviation of point elevation within a 1.5 m radius, showing increasing error with increasing variability. A random sample of 10,000 points was chosen for display while the analysis was carried out on the entire point cloud (62,873,538 and 108,916 points for 2020 and 2019 respectively). b) Standard deviation of error within 100 classes of topographic variability shows strong linear relationships with topographic variability.

4. Results

4.1 Subsidence activity on the floodplain

In the area surrounding Ripon Loop, the mapping of the sinkholes shows several clusters labelled A-D in Figure 7. These clusters lie at the margins of the buried valley and the adjacent more elevated bedrock. Area A lies to the west of the buried valley and comprises a golf course where care had to be taken to differentiate the sinkholes from the man-made features including bunkers. The aerial photography was used for this in addition to the lidar.

The golf course area has some large and very pronounced sinkholes, many conical in shape; there is also a record of an active subsidence here in 1860 (Cooper, 1986) and presently active ground tilting is noted on greens near the river.

Area B includes three adjacent sinkholes forming the row of Corkscrew Pits and many large well-developed sinkholes, some of which have been active in historical times, that form lines through Hutton Conyers. Area C at Hall Garth Ponds also included a row of 3 adjacent sinkholes that were highly visible on maps and photographs up to 1986, but which have subsequently been enlarged by excavation to extend the ponds. An active subsidence occurred in the woods here in 1939. This collapse left a water-filled crater 30 m across and 7 m deep (Cooper, 1986) from which sulphate-rich spring-fed water flows (Cooper et al., 2013). Bedrock of the Brotherton Formation is exposed in the back of this hole showing rock at surface here forming the eastern flank of the buried valley. Area D is composed mainly of subdued sinkholes that have been smoothed by agriculture, but is still active as shown by a sinkhole visible on some maps (1938 and 1957) and the 2002 aerial photography, and obviously filled in on intervening and later datasets (this hole is located 431220,474055 just south of the letter D in Fig. 7).

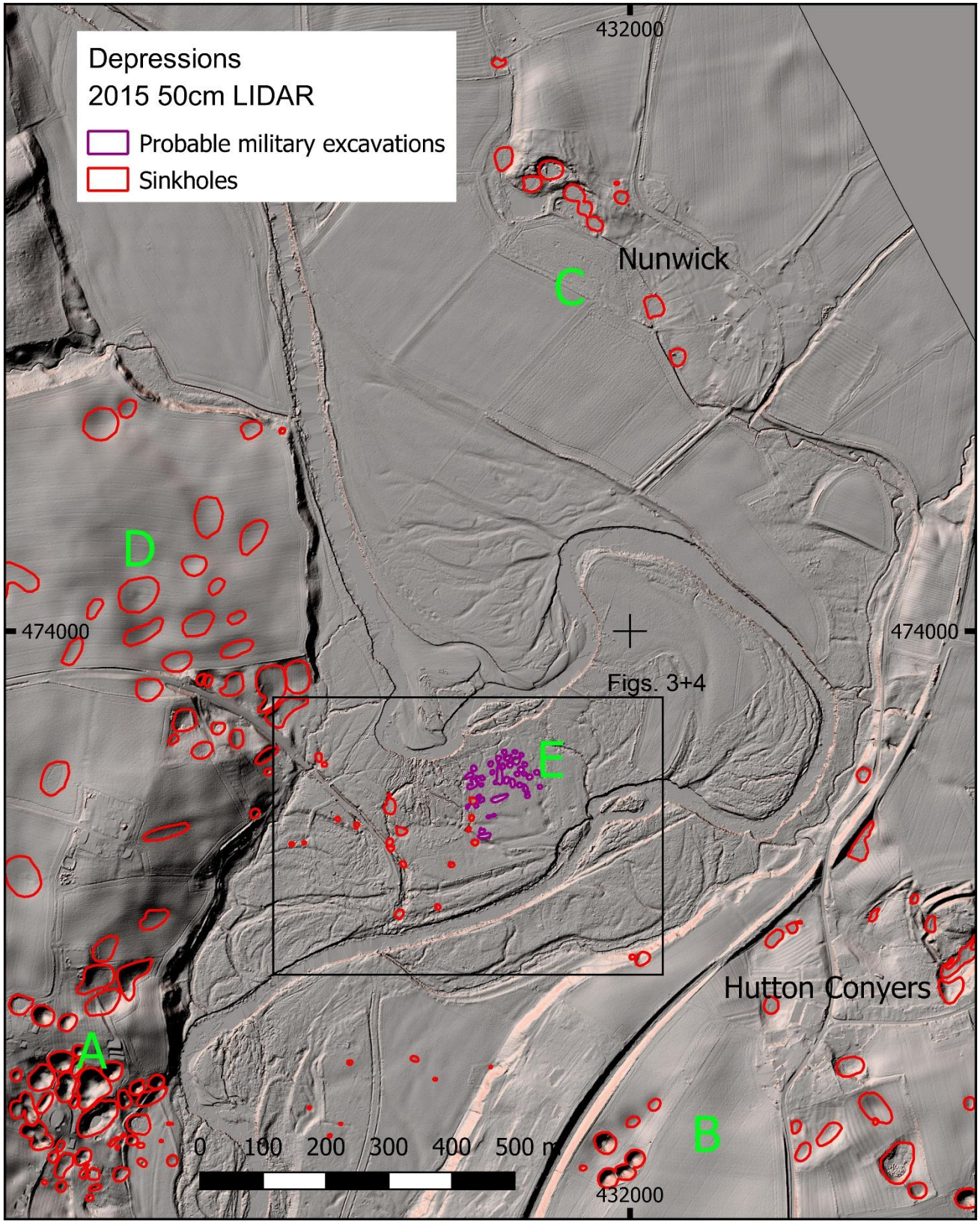

Figure 7 Environment Agency 2015 50 cm lidar processed in hill shade and slope combined in QGIS to show sinkholes and probable military excavations. The areas A to E are discussed in the text. The extent of Figures 3 and 4 is outlined. Contains Environment Agency information © Environment Agency and/or database right 2021.

Area E differs from A to D as it is situated on the alluvial deposits of the River Ure. This area was a military training ground prior to becoming a nature reserve. It is unclear when it started to be used for military training, but Ripon was a major camp for both world wars. The western part where sinkholes have developed and the river has cut through is discussed in more detail below. The eastern part of area E has mainly military excavations that are well-displayed in Figure 3 and 4, but there is also a line of sinkholes (G10-G11 in Fig. 8) with G10 dating back to 1856. One feature that distinguishes sinkholes from the military excavations is that the latter commonly have a raised rim or mound on the defensive side where material has been dug out, many of these can be seen on the 2015 lidar data. Some explosion and bomb craters can also have a raised rim, but these quickly become degraded (Tunwell et al., 2016); both sinkholes and bomb craters can have similar dimensions. Ripon was the base for the Royal Engineers and Military Engineers Bomb Disposal School from 1941 onwards and it is possible that cratering may also be related to their activities. There is a slight, but unlikely, possibility that there may also be bomb craters, but Ripon was only bombed once 02/01/1941-03/01/1941 and other records are for Mickley and Darrogill respectively 7 and 13 km away with no documentary evidence for Ripon Loop or Nunwick (Blomvall, 2019).

In more detail, sinkholes within area G are shown with sequential date information in Figures 8 and 9. The western part of Ripon Loop where the River Ure has cut through in 2019 has been the focus for sinkhole development that has strongly influenced the river's change of course, notably groups of sinkholes G2-G9.

Group G1 lies on the flood plain outside of the new chute channel. It shows a long-lived sinkhole present as one of several elongate ponds connected by a stream to the River Ure in the 1890s, but developed at its northern end into a circular sinkhole visible on all the datasets from 2009-2018. South-east of this there is another sinkhole visible in 2009 and 2015 and a further two south-east of that both visible on the 1986 dataset. These hollows form a line parallel to the edge of the alluvium and buried valley which is also approximately in line with group G2.

Group G2 is first recorded as a pond on the 1909 dataset and shown with the same outline until 1957. The 1968 dataset has a similar outline, but is ~6 m further south. This may be a map registration issue, similarly for the 1986 dataset. The 2001 lidar shows a larger SW-NE trending oval depression with another circular depression to the north. By the time of the 2009 lidar, both holes had grown in size and were both visible on the 2011 dataset. The

2015 lidar showed a different configuration with both holes merged into an irregular drop shape; the shape is similar in 2017. By 2018 it had a similar size, but the hole in the north had developed more and abutted the main hole; the 2019 image showed the main hole to be the same, but the northern one enlarged. This hole illustrates the growth from a small hole to a large one and the formation of another sinkhole next to it.

Group G3 is first recorded as a pond on the 1892 dataset and shown with the same outline to 1957. The 1968 outline is smaller and may reflect partial filling of the hole. The 1986 data show an enlargement of the hole from 1968 and development of an irregular depression to the north which has formed into a larger depression on the 2001 lidar, while the main hole has expanded to the north-east. The 2009 lidar shows these two areas amalgamated into one large hollow, a pattern repeated on all the subsequent datasets with minor variations to 2019. Immediately west of the main hole a new sinkhole feature is visible on the 2017-2019 data, but not the 2015 lidar where only a narrow channel is shown, thus it appears to have subsided post this date (Fig. 10c).

Group G4 is visible on the data from 1986 and all three lidar datasets from 2001, 2009 and 2015. It is not clearly visible on the aerial photography where it is obscured by trees. It shows a sinkhole in approximately the same position on all datasets with another to the north-west on the 2009 and 2015 data, plus one to the south east on the 1968 map. These three holes form an approximately NW-SE trending line continuing into the G5 group.

The G5 group forms the northern end of a chain of hollows labelled G6, G7 and G8. At distinct dates most of the hollows are separated, but subsequent collapses tend to expand the hollows or occur in the intervening ground. Group G5 is first seen as a sinkhole in 2002, by 2009 it has grown slightly and another hole appeared adjacent to the north. By 2015 this had grown so both holes were similar in size at about 10 m across. By 2017 only the northern hole was clearly visible and the southern one was partly obscured. 2018 saw the northern one expand slightly and another hole appear to the north-east of the original southern hole. This additional hole was subsequently subsumed by expansion of the northern hole seen on the 2019 data.

The G6 cluster first became visible on the 2011 aerial photograph, and was present, but slightly larger on the 2015 lidar. By 2017 it had expanded to the NNW becoming elongate in shape, and this expansion continued as shown on the 2018 and 2019 photographs when it had expanded to touch the G5 group.

The G7 sinkholes follow a similar trend. In 1968 a north-south trending elongate pond is shown, while in 1986 only the northern part of this is visible, but the 2001 lidar delineated the whole pond area. By the time of the

2009 lidar only the northern part was visible, and it had expanded slightly northwards where it abuts the G6 group described above.

The G8 group formed as a sinkhole in 2018 to the south of G7. By 2019 it had grown northwards to overlap with the area of the 1968 G7 hole. It is possible that the southern sinkhole in this group was filled with sediment between 2018 and 2019.

The most southerly sinkhole is G9 which is present on both the 2009 and 2015 lidar but is obscured by trees on the photographs.

The groups of sinkholes from G5 to G8 form a chain of sinkholes that at various times overlap to form a continuous slightly sinuous row with an approximately north-south orientation (Figures 8 and 9). Groups G2 and G3 form large clusters just to the north of this. The cumulative area of the sinkholes within the zone later affected by the chute cutoff has increased more than three-fold from 303 m^2 in 1968, over 387 m^2 and 931 m^2 in 1986 and 2001 respectively, to 1048 m^2 in 2009. This figure dropped to 878 m^2 on the 2015 lidar dataset but has increased to 1366 m^2 on the 2019 aerial photo despite tree canopies obstructing the view on the full extent of some features.

Lying to the east of G1-G9 there is another line of sinkholes, the northern one labelled G10 and the remainder of the group G11 (Fig. 8). Hole G10 was first shown as a pond on the 1856 map. It was subsequently left off any maps, but a feature was present overlapping with it on all the datasets from 1986 to 2019. Given that the accuracy of the first series of six-inch to one mile (1:10,560) scale maps was not as accurate as later maps, it is highly probable that this is the same feature. In a similar way all of the sinkholes in group G11 are present on all the datasets from 2001 to 2019, though only half of them were recognised in 1986. In contrast to the groups to the west, these sinkholes have remained more or less in the same positions throughout their existence.

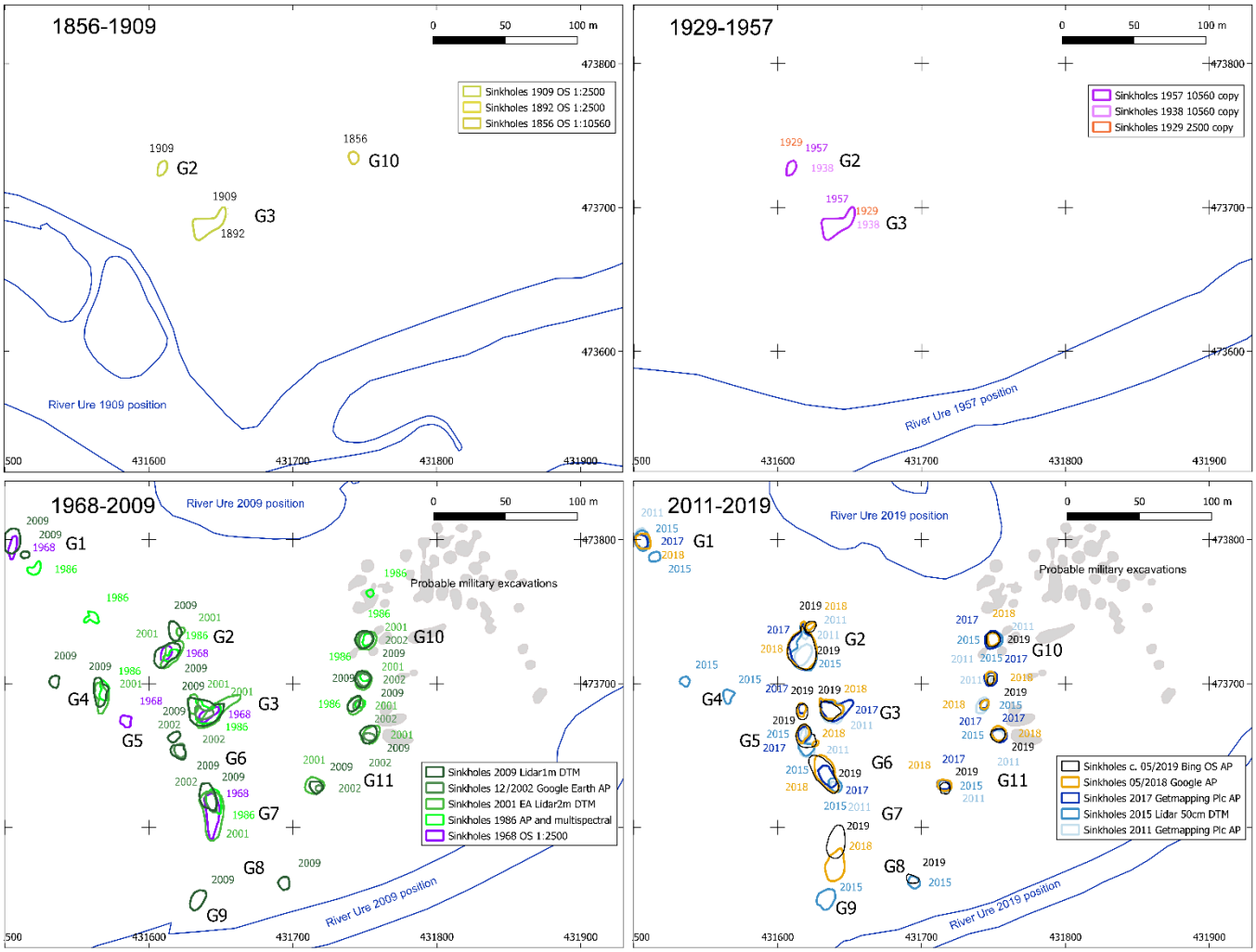

Figure 8. Sinkholes shown by dataset age on which they are recognised. Groups G1 to G11 are discussed in the text.

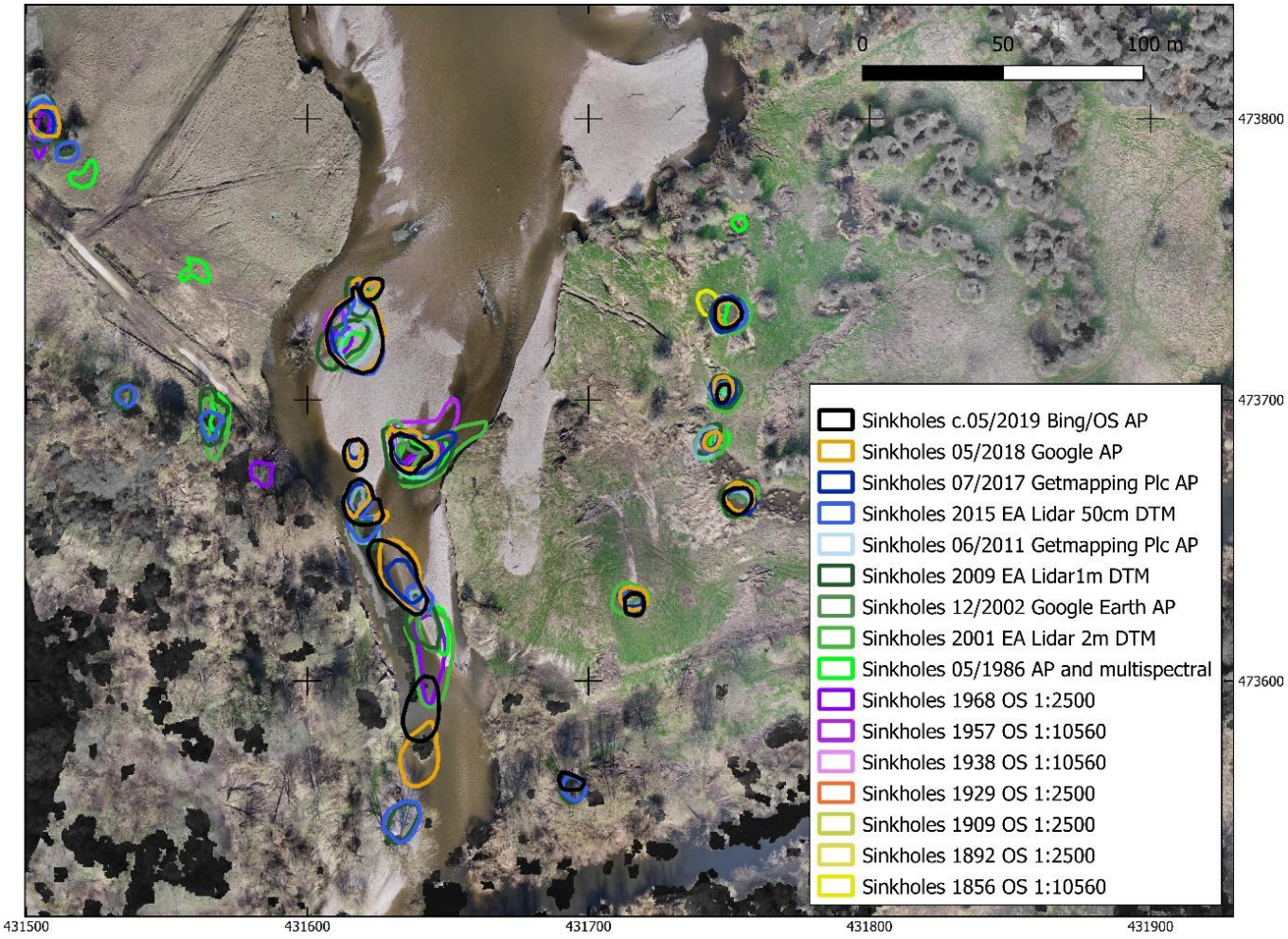

Figure 9. Locations and dates of sinkholes from map, aerial photography, lidar and multispectral data as shown in legend and detailed in Table 1; base topography March 2020 orthophotograph with blanks filled by dark grey.

4.2 Cutoff process

Since the early 20th century, the Ripon Loop compound bend has experienced down-valley translation and anti-clockwise rotation (Fig. 2) and has reached a sinuosity of 1.8 in 2019. This creates a significant gradient advantage for any overbank flows across the neck of the bend. Overbank flows have been particularly common in the hydrological years 2000-2002, 2007, 2008, 2016 and 2020, and aerial photos and lidar data provide evidence for superficial erosion by such overbank flows across the neck of Ripon Loop since 2012 (Fig. 10b). An increase in the areal extent of mostly water-filled depressions in this part of the floodplain over the last 50 years (Figs. 8 and 9) as well as the formation of numerous new sinkholes (e.g. G2, G3 and G5) indicate subsidence activity along the edge of the buried valley. While most of these depressions are likely associated with sinkhole activity, the small

embayments on the northern edge of some sinkholes (e.g. G2, G3 and G5) as well as narrow channels connecting them at a superficial level from 2015 show that headward incision during periods of overbank flow might have extended them as well (Fig. 10a,c). Gravel deposited by these overbank flows at the southern end of sinkholes has temporarily decreased observed sinkhole dimensions (e.g. G3, G5 and G8). By summer 2019 the sinkholes in the southern part of what became the cutoff channel (Fig. 2) had partially connected via headward erosion with low-level thresholds in between (Fig. 10c). As Ripon Loop has translated down-valley since the 1900s, the lower part of this chute channel has incised easily into relatively unconsolidated, less than 170 year old channel deposits (Fig. 2) which were well exposed in the sinkholes (Fig. 10c,d).

During late summer and autumn 2019 numerous flood events occurred and already during the first of five floods between 27th September and 11th October fast-flowing, channelised flow of several metres width across the neck was observed although flow depth was limited (Supplementary video S1) and the majority of discharge was still routed through the meander bend. The following floods widened the channel by the end of October to more than 10 m in most places apart from the uppermost 100 m where two smaller channels persisted (Supplementary video S2). The depth at the head of the chute had increased to the effect that the new channel was largely water-filled at below bankfull discharge. However, the angle of approach in the upstream bend and protection by the remnants of a dissected point bar meant that little flow was attracted (Supplementary video S2). As the hydrograph in November was characterised by only five spates, it is most likely that four successive floods between 6th and 12th December finally increased chute channel capacity sufficiently to attract the majority of the discharge compared to the meander loop. Anecdotal evidence from local landowners indicates that water level in the latter fluctuated considerably over the following weeks which suggests substantial sediment dynamics at its upstream connection with the new channel. Photographic evidence from early January 2020 suggests substantial sedimentation in the upper 200 m of the abandoned channel and shows a very straight chute channel that conveyed all surface discharge. More substantial floods followed until 20th March, particularly during February, during which the new channel has widened. Hereby the western bank has been eroded in particular, and dynamic channel adjustment occurred resulting in persistent bars, incorporation of large woody debris and increase in low flow channel curvature (Fig. 5).

Figure 10. Photos of Ripon Loop before cutoff (April 2019). (A) View in northerly direction towards sinkhole group G2 with superficial erosion channel from overbank flows in the foreground. (B) View in southerly direction from the head of the future chute channel towards sinkhole group G2 (same fallen tree in top right as visible in panel A) showing multi-thread superficial erosion scoured by flood waters since 2012. (C) New sinkhole subsided after 2015 associated with group G3 and group G5 in the background viewed from the same position as the photo in panel A but in south-westerly direction. Cobbles from overbank flows are visible at the downstream end and on floodplain in the foreground. Thick channel deposits are exposed on the edge of G5 while a thin cemented layer of cobbles at shallow depth is visible in the bottom right. (D) View in southerly direction on the chain of partly coalesced sinkhole groups G5 to G8 with cobbles deposited in the down-valley end of G6 and finer sediment in the southern part of G5 in the foreground. Sinkholes groups are defined in Fig. 8.

4.3 Sediment mobilisation and topographic change

The establishment of the cutoff channel led to the downstream extension of the remnants of a gravel point bar in the bend upstream, which had been dissected after 2015 (Supplementary video S2). The eastern tail of this bar had by March 2020 almost blocked off the former channel to the abandoned meander bend (Fig. 2) and a new shallow and aggrading channel had formed further north to connect to the meander bend (Fig. 5). The former channel on the outside of the former bend upstream of the cutoff has narrowed and the main flow is in the centre of the cutoff channel. As the latter widens further downstream flow is diverted in approximately equal parts around a mid-channel bar, hereby eroding the western bank. The comparison of the pre- and post-cutoff DEMs after application of the LoD (Fig. 11) clearly identifies the incised channel with particularly high vertical erosion and deep scour of up to 3 m depth on the higher western bank. As the channel at the toe of this western bank is waterfilled over almost its entire length (Fig. 5) comparison was thus made to the water surface which represents an underestimation. Nevertheless, the reduction in erosion towards the cutoff channel centre indicates patterns of overbank flow scour prior to cutoff.

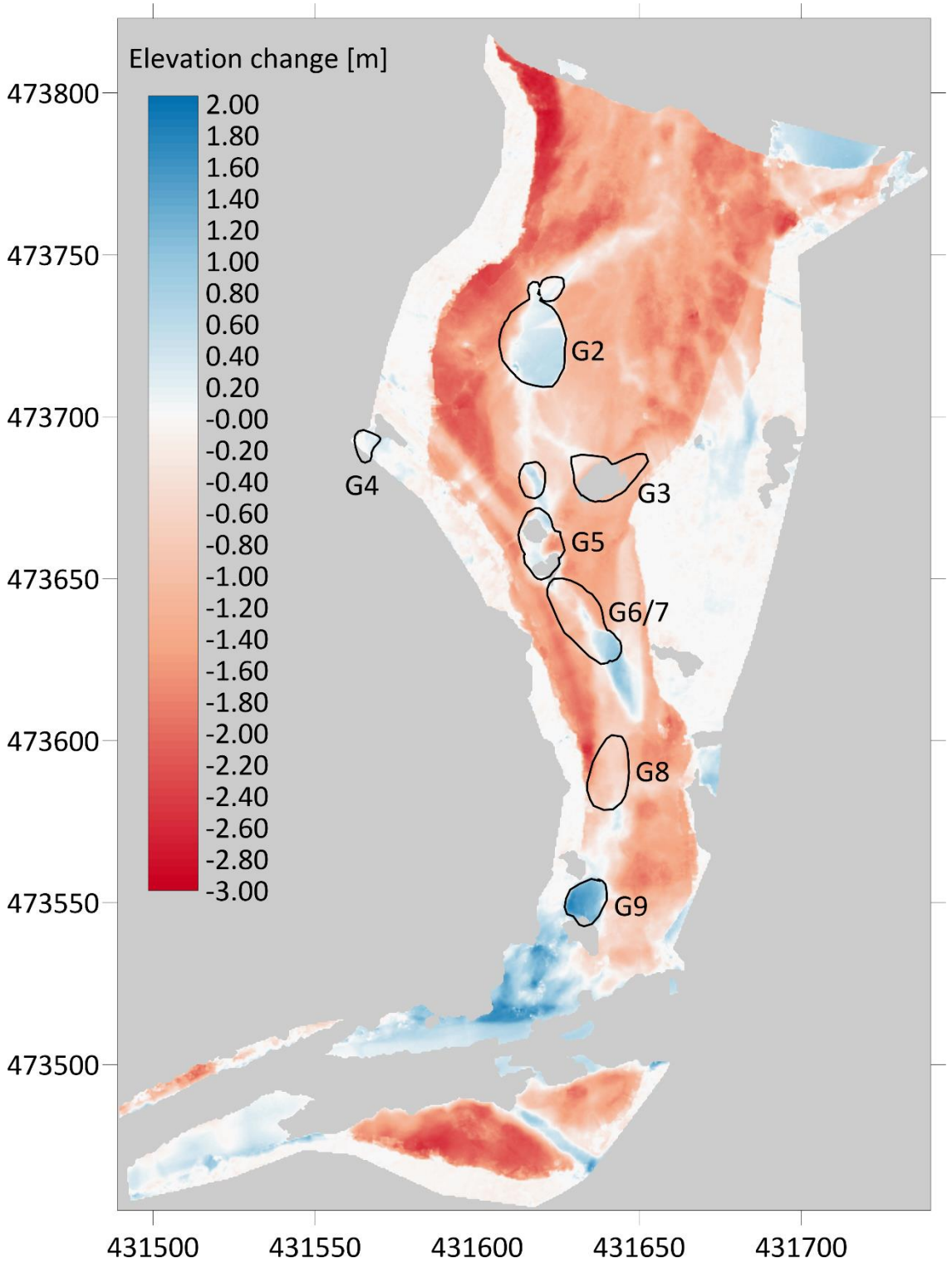

Figure 11. Topographic differences (in metres) within the study area from DEMs prior to cutoff and post-cutoff after application of the spatially variable level of detection. Depressions in floodplain likely associated with subsidence since 2015 are outlined and labelled as in Fig. 8. British National Grid coordinates are in metres.

Areas associated with sinkholes (Fig. 11) have mostly experienced deposition, even when their pre-cutoff surface represented the water level in the sinkholes. Sinkholes G2, G7 and G9 (Fig. 8) are now covered in thick bar

deposits (up to 0.6 m, 1.1 m and 1.8 m fill respectively) while sinkholes G3, G5, G6 and G8 are now representing topographical lows such as the channel thalweg where in places the presence of water surfaces in both DEMs prevented comparison.

Downstream of the mid-channel bar flow is focused on the eroding western bank (Fig. 3) where remnants of the service track provide some resistance to erosion. The chute channel narrows to the south with several bars developing. Towards the true right end of the chute channel deposition of up to 2 m is dominant, where an emerging point bar is establishing itself and has filled parts of the old channel. In contrast, on the opposite (southern) side of the channel substantial bank erosion of up to 25 m horizontally has created space for the accommodation of this new bend. The proximal channel downstream is dominated by deposition in form of bars.

The volumetric difference between the two DEM surfaces is -18318 m^3 with 71% of area experiencing erosion of 20422 m^3 and 2104 m^3 of deposition in the remaining area (Table 2). The uncertainty of the detected topographical changes as assessed to a 95% confidence level is highest at breaks in slopes, particularly influenced by river banks in the 2020 DEM where the LoD can reach values of up to 1.4 m (Fig 12). Bar edges, low vegetation and accumulations of driftwood provide other areas of uncertainty. Application of the LoD reduced the area where erosional topographic change could be discerned by 617 m^2 and areas affected by deposition showed higher uncertainty and thus these volumes were reduced to a larger extent (-17.4% versus -6.2% for volumes of erosion).

Table 2. Topographic change associated with the chute cutoff at Ripon Loop, River Ure between October 2019 and March 2020. The uncertainty of the detected topographical changes is captured at the 95% confidence level through a 'Level of Detection' (LoD).

	Volume after application of LoD [m^3]	Relative reduction in volume by LoD in %	Area after application of LoD [m^2]
Erosion	-20422	-6.2	20005
Deposition	2104	-17.4	8232
Total	-18318	-4.8	28237

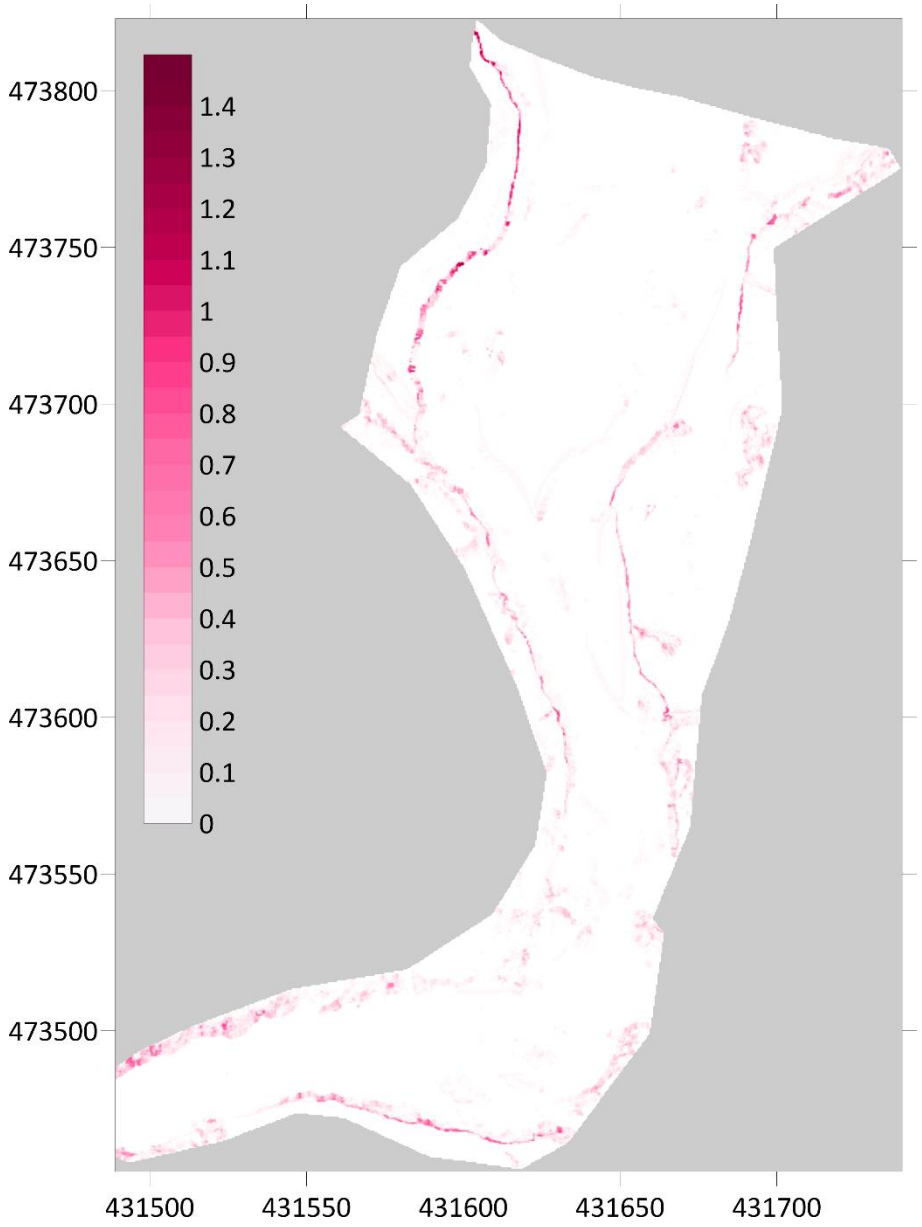

Figure 12. Spatial distribution of the uncertainty to detect topographic change at 95% confidence level (given in metres and referred to as 'level of detection') that arises from the propagation of the spatially variable error associated with the used DEMs. British National Grid coordinates are in metres.

5. Discussion

The sinkholes at Ripon Loop have behaved in the two different ways described by Cooper (1986). The first type (G4, G10, G11 in Fig. 8) have long-lived sinkhole activity where the hole continues to collapse and keeps more or less the same size and position. In this circumstance it is likely that material collapsing down the hole is being washed away underground maintaining the sinkhole at the surface. The second situation (G1, G2, G3, G5-G8 in Fig. 8) is where collapses occur and effectively choke up the cave/cavity underground causing the groundwater

flow to dissolve the adjacent ground. In this situation adjacent rows of sinkholes can occur such as those seen at Corkscrew Pits and Hutton Conyers (B in Fig. 7) or those at Hall Garth Ponds, Nunwick (C in Fig. 7). At Ripon Loop, the changes in shape and movement of the sinkholes in the area that was subsequently eroded by the new channel suggests the latter mechanism.

The alignment of the rows of sinkholes is related to four aspects of the geology. As previously demonstrated by Cooper (1986), there is a strong correlation between the joint pattern in the bedrock and the pattern of subsidence that tends to occur at the intersections of the approximately north-south and east-west trending joint sets giving lines of hollows with these trends. In addition, he recognised diagonal lineations related to the reticulate cave pattern. The second influence is the orientation of the buried valley that is controlled by the regional geological dip and outcrop of the strata (Cooper, 1998). This tends to have a NNW-SSE strike followed by the buried valley, but it is modified by faulting to the south of Ripon Loop where the buried valley narrows and curves past Ripon. The third influence is the water flow from the adjacent and interbedded aquifers into the gypsum, then into the overlying superficial deposits in the buried valley, where sulphate-rich spring activity is common (Cooper et al., 2013). All these features are seen controlling the sinkholes at Ripon Loop. Spring activity and water flow from the gypsum into the buried valley is also evidenced by the presence of tufa-cemented gravels beneath Ripon Loop and further south (Morigi and James, 1984; Cooper et al., 2013). The tufa is deposited from sulphate and carbonate-rich waters emanating from the dolostone/limestone and gypsum aquifers under artesian pressure. A fourth factor, not previously elaborated, is the shallow groundwater flow in the gravels of the buried valley. This will have a similar hydraulic gradient to that of the river and an overall southerly flow. The situation at Ripon appears very similar to that described by Seyoum and Eckstein (2014, Figures 10 and 12) and Morgan et al. (2019). In places the buried valley deposits will have sulphate-rich water from the bedrock spring activity, but sulphate-poor river water that infiltrated upstream will also contribute to the flow and be aggressive, likely causing the dissolution of gypsum at rockhead in the valley bottom. This fourth mechanism would explain some of the migration of sinkholes, in lines progressing in the axial direction of the buried valley, that subsequently became the chute channel.

The collected data show a significant increase in the areal extent of the sinkholes that were located in the zone now occupied by the chute channel over the last 40 years. While some of this may be attributed to the resolution and type of the older datasets, the magnitude as well as the formation of new sinkholes suggest an increase in

subsidence activity. Smaller sinkholes have coalesced and a tendency of NNW extension of existing sinkholes has been observed (G5-G8). An equal extension in the opposite direction following the edge of the buried valley might be masked though by deposition of fluvial bedload during frequent overbank flows in the southern parts of these depression. Conversely, the northward extension might be partly caused by headward incision driven by the high gradient advantage (> 2 m over the 280 m neck of the meander bend). Particularly, the narrow and often shallow extensions of G2 and G3 are aligned with recent and older scour channels from overbank flows (Figs. 3 and 4). Field observations from 2019 show that overbank flow is focussed radially from upstream into these depressions which concentrates stream power on small areas. Accelerated headward incision by funnelling relatively shallow overbank flows into one headcut has been observed at chute cutoffs (Gay et al., 1998; Zinger et al., 2011). The effects of headward incision at Ripon Loop are more pronounced at the southern part of the cutoff (South of G5) where the less than 170-year-old channel gravel deposits might have provided increased sub-surface water percolation and decreased resistance to erosion. In contrast, the outline of the initial chute channel in the northern part was strongly conditioned by the location of long-lived sinkholes (particularly G2 and G5, Fig. 9) and headward incision was impeded by cohesive floodplain sediments and, between G2 and G5, also a layer (10-20 cm) of cemented rounded and sub-rounded gravels (Fig. 10c). Whether the latter is a shallow tufa deposit or of anthropogenic (military) origin could not been established before the cutoff occurred.

A further influence of the river on sinkhole formation is the triggering of collapses during and after flood events by sudden changes in water levels washing materials down into cavities, or causing collapse due to changes in hydrostatic support. These are triggering mechanisms, both natural and man-made, that are well-documented in karst areas (Hyatt and Jacobs, 1996; Waltham et al., 2005; Gutiérrez et al., 2014). Another factor that affects the sinkhole pattern is the filling of sinkholes on the floodplain during flood events making some holes effectively "disappear" from later datasets.

The volume of sediment mobilised by chute cutoffs can exceed that associated with bank erosion from lateral migration by up to five orders of magnitude (Zinger et al., 2011) and as such create significant sediment pulses with effects on downstream morphodynamics and habitats, but also anthropogenic infrastructure and commodities. At Ripon Loop >20000 m^3 have been eroded within the first phase of chute cutoff hereby producing similar volumes as those reported from other piedmont chute cutoffs in the UK, e.g. 15000 m^3 at the River Coquet over 21 months (Fuller et al., 2003), although there erosion in the first 4 months after cutoff was a much lower

1864 m^3 compared to Ripon Loop. The calculated volumetric change at Ripon contains elements of overestimation as well as underestimation. The lack of bathymetric data for deep water required a conservative estimate of erosion to an interpolated water level (or shallow water depth level where the water surface was smooth). The water of the River Ure is stained brown due to the drainage of peatlands and as such water transparency was limited during the survey in March 2020. Spatially variable discoloration rendered the use of a single refraction coefficient impracticable and thus no attempt was made to extend the depth range of the photogrammetric survey (Woodget et al., 2015). Deep water was found mainly in the channel upstream of the cutoff and in the lower part of the cutoff channel. Conversely, the deposition over open water on the pre-cutoff DEM represents an underestimation because the fill volume between 2019 sediment surface and water level is not accounted for. However, this concerns only smaller areas of the study area such as infilled sinkholes (Fig. 11). The use of the 2015 lidar dataset for the pre-cutoff floodplain surface provides some uncertainty in the volumes calculated because subsidence, deposition in sinkholes and floodplain erosion from overbank flows between March 2015 and October 2019 are included. However, aerial imagery and field visits indicate that erosion and sinkhole growth was to some extent balanced by gravel deposits in this period and the largest difference, the cutbank erosion in the upstream bend was accounted for by using the 2019 bank line.

Within the framework of known mechanisms of alluvial chute cutoff, this example presents a combination of allogenic influence of gypsum sinkholes and autogenic processes such as headward incision by overbank flows (Constantine et al., 2010). As such it can be associated with Viero et al. (2018)'s macro-group of chute cutoffs that are controlled by a gradient advantage of preferential flow paths across the floodplain, with local gradient exacerbated by the presence of sinkholes. The small radius of curvature of the upstream bend prior to cutoff (Fig. 2) and the almost perpendicular approach of flow across the dissected point bar to the neck of the bend (Supplementary video S2) might have, in absence of sinkholes, facilitated a larger influence of direction and inertia of channelised flow on potential cutoff formation compared to the gradient advantage across the neck but whether this would have been sufficient to trigger a chute cutoff at this point is questionable.

6. Conclusions

This study outlines the spatial extent of collapse sinkholes on Ripon Loop over the past 164 years, with particular focus on their formation in alluvial floodplain deposits hereby extending previous studies. Two populations of sinkholes can be distinguished by their long-term behaviour. The first group is long-lived in that subsidence is not balanced by fluvial overbank deposition with a limited scope for areal expansion, while the second group is dominated by new activity, growth and coalescence with neighbouring holes and aligned with the edge of the buried valley. At Ripon Loop large and long-lived sinkholes G2 and G3 are associated with the capture of overbank flows which in turn promotes subsequent headward erosion and formation of shallow proto-chute channels that connect between sinkholes and the upstream bend. As such their presence has clearly defined the early course of a developing chute cutoff and fluvial processes, which driven by locally steep gradients has modified the subaerial shape of the sinkholes by erosion and deposition. Younger and more dynamically growing sinkholes (G5-G9) of the second group have extended the chute channel further towards the lower limb of the meander bend. Their evolution suggests accelerated dissolution by groundwater around choked initial cavities. This leads to the interesting question as to what extent the river-fed groundwater flows in the alluvial and buried channel bodies interact with the artesian head of groundwater and the implication for sinkhole activity and thus river channel dynamics. While this is beyond the scope of this study, hydrogeological investigation could provide insight into the feedback mechanisms created in such a system. During a flood-driven cutoff process that required several events to capture the majority of the flow in the new channel, the latter was widened gradually and eroded more than 20000 m^3 of floodplain with only ~2100 m^3 of deposition in the study area. Deposition was mainly in sinkholes and the lower end of the reach. While the fate of the mobilised material in regard to downstream infrastructure and habitats should be investigated, the question how the active sinkholes interact with morphological adjustment in the new channel is of considerable interest. This research evidences the influence of processes allogenic to the fluvial system on channel dynamics and thus provides another dimension to the array of chute cutoff mechanisms described in previous studies.

Acknowledgements

The research was supported by allowing site access and the provision of aerial and terrestrial photography made available by the Yorkshire Wildlife Trust. Flow and stage data was provided by the Environment Agency. We thank

Chris Osborne and David Powell for permitting the use of video footage from September and October 2019. The helpful comments from Vanessa Banks (British Geological Survey), Jo De Waele and Ian Fuller have improved the manuscript. AHC publishes with the permission of the British Geological Survey Chief Scientist for multihazards and resilience (UKRI-NERC).

References

Ahmed, J., Constantine, J., Dunne, T., 2019. The role of sediment supply in the adjustment of channel sinuosity across the Amazon Basin. Geology 47.

Ashmore, P.E., 1991. How do gravel-bed rivers braid? Canadian Journal of Earth Sciences 28(3), 326-341.

Benito, G., Gutiérrez, F., Pérez-González, A., Machado, M.J., 2000. Geomorphological and sedimentological features in Quaternary fluvial systems affected by solution-induced subsidence (Ebro Basin, NE-Spain). Geomorphology 33(3), 209-224.

Benito, G., Pérez-González, A., Gutiérrez, F., Machado, M.J., 1998. River response to Quaternary subsidence due to evaporite solution (Gállego River, Ebro Basin, Spain). Geomorphology 22(3), 243-263.

Blomvall, L., 2019. Bombing Britain: an air raid map - Warstateandsociety.com web pages.

Brasington, J., Langham, J., Rumsby, B., 2003. Methodological sensitivity of morphometric estimates of coarse fluvial sediment transport. Geomorphology 53(3-4), 299-316.

Brasington, J., Rumsby, B.T., McVey, R.A., 2000. Monitoring and modelling morphological change in a braided gravel-bed river using high resolution GPS-based survey. Earth Surface Processes and Landforms 25(9), 973-990.

Braudrick, C.A., Dietrich, W.E., Leverich, G.T., Sklar, L.S., 2009. Experimental evidence for the conditions necessary to sustain meandering in coarse-bedded rivers. Proc Natl Acad Sci USA, 106(40), 16936-16941.

Bridge, J., Smith, N., Trent, F., Gabel, S., Bernstein, P., 1986. Sedimentology and morphology of a low-sinuosity river: Calamus River, Nebraska Sand Hills. Sedimentology 33(6), 851-870.

British Geological Survey, 1987a. Harrogate, England and Wales Sheet 62. Drift Geology. 1:50,000. Ordnance Survey, Southampton for the British Geological Survey.

British Geological Survey, 1987b. Harrogate, England and Wales Sheet 62. Solid Geology. 1:50,000. Ordnance Survey, Southampton for the British Geological Survey.

British Geological Survey, 1992a. Thirsk, England and Wales Sheet 52. Drift Geology. 1:50,000. Ordnance Survey, Southampton for the British Geological Survey.

British Geological Survey, 1992b. Thirsk, England and Wales Sheet 52. Solid Geology. 1:50,000. Ordnance Survey, Southampton for the British Geological Survey.

British Geological Survey, 1996. Ripon. England and Wales Sheet SE37SW.Bedrock and Drift 1:10,000. British Geological Survey, Keyworth, Nottingham.

Camporeale, C., Perona, P., Porporato, A., Ridolfi, L., 2005. On the long-term behavior of meandering rivers. Water Resources Research 41, W12403.

Camporeale, C., Perucca, E., Ridolfi, L., 2008. Significance of cutoff in meandering river dynamics. Journal of Geophysical Research: Earth Surface 113(F1).

Castañeda, C., Gutiérrez, F., Manunta, M., Galve, J.P., 2009. DInSAR measurements of ground deformation by sinkholes, mining subsidence, and landslides, Ebro River, Spain. Earth Surface Processes and Landforms 34(11), 1562-1574.

Constantine, J.A., Dunne, T., 2008. Meander cutoff and the controls on the production of oxbow lakes. Geology 36(1), 23-26.

Constantine, J.A., Dunne, T., Ahmed, J., Legleiter, C., Lazarus, E.D., 2014. Sediment supply as a driver of river meandering and floodplain evolution in the Amazon Basin. Nature Geoscience 7(12), 899-903.

Constantine, J.A., McLean, S.R., Dunne, T., 2010. A mechanism of chute cutoff along large meandering rivers with uniform floodplain topography. Geological Society of America Bulletin 122(5-6), 855-869.

Cooper, A.H., 1986. Subsidence and foundering of strata caused by the dissolution of Permian gypsum in the Ripon and Bedale areas, North Yorkshire. In: G.M. Harwood, D.B. Smith (Eds.), The English Zechstein and Related Topics. Geological Society Special Publication. Geological Society, London 22(1), pp. 127-139.

Cooper, A.H., 1989. Airborne multispectral scanning of subsidence caused by Permian gypsum dissolution at Ripon, North Yorkshire. Quarterly Journal of Engineering Geology and Hydrogeology 22(3), 219-229.

Cooper, A.H., 1998. Subsidence hazards caused by the dissolution of Permian gypsum in England: geology, investigation and remediation. In: J.G. Maund, M. Eddleston (Eds.), Geohazards in engineering geology. Geological Society of London, London, pp. 265-275.

Cooper, A.H., 2020. Geohazards caused by gypsum and anhydrite in the UK: including dissolution, subsidence, sinkholes and heave. In: D.P. Giles, J.S. Griffiths (Eds.), Geological Hazards in the UK: Their Occurrence, Monitoring and Mitigation – Engineering Group Working Party Report. Engineering Geology Special Publications. Geological Society, London, pp. 403-423.

Cooper, A.H., Burgess, I.C., 1993. Geology of the Country Around Harrogate. Memoir for 1:50000 geological sheet 62 (England and Wales). H.M. Stationery Office, London.

Cooper, A.H., Odling, N.E., Murphy, P.J., Miller, C., Greenwood, C.J., Brown, D.S., 2013. The role of sulfate-rich springs and groundwater in the formation of sinkholes over gypsum in Eastern England. In: L. Land, D.H. Doctor, J.B. Stephenson (Eds.), Sinkholes and the Engineering and Environmental Imapacts of Karst: Proceedings of the Thirteenth Multidisciplinary Conference, May 6-10. . National Cave and Karst Research Institute, Carlsbad, New Mexico, pp. 141-150.

Daxter, C., 2020. Topographic Openness Maps and Red Relief Image Maps in QGIS, University of Innsbruck, Institute of Geology.

Dean, D.J., Schmidt, J.C., 2013. The geomorphic effectiveness of a large flood on the Rio Grande in the Big Bend region: Insights on geomorphic controls and post-flood geomorphic response. Geomorphology 201, 183-198.

Doctor, D.H., Young, J.A., 2013. An evaluation of automated GIS tools for delineating karst sinkholes and closed depressions from 1-meter Lidar-derived digitial elevation data. In: L. Land, D.H. Doctor, J.B. Stephenson (Eds.), Sinkholes and the Engineering and Environmental Imapacts of Karst: Proceedings of the Thirteenth Multidisciplinary Conference, May 6-10. National Cave and Karst Research Institute, Carlsbad, New Mexico, pp. 449-458.

Doğan, U., 2005. Land subsidence and caprock dolines caused by subsurface gypsum dissolution and the effect of subsidence on the fluvial system in the Upper Tigris Basin (between Bismil–Batman, Turkey). Geomorphology 71(3), 389-401.

Doneus, M., 2013. Openness as visualization technique for interpretative mapping of airborne Lidar derived digital terrain models. Remote Sensing 5, 6427-6442.

Eekhout, J.P.C., Hoitink, A.J.F., 2015. Chute cutoff as a morphological response to stream reconstruction: The possible role of backwater. Water Resources Research 51(5), 3339-3352.

Fares, Y., Herbertson, J., 1990. Partial cut-off of meander loops a comparison of mathematical and physical model results. W.R. White (Ed.). Proc. Int. Conf. on River Flood Hydr, Wallingford, pp. 289-297.

Fisk, H.N., 1947. Fine-grained alluvial deposits and their effects on Mississippi River activity. USCE Mississippi River Communications 1, 82.

Frascati, A., Lanzoni, S., 2010. Long-term river meandering as a part of chaotic dynamics? A contribution from mathematical modelling. Earth Surface Processes and Landforms 35, 791-802.

Fuller, I.C., Large, A.R.G., Milan, D.J., 2003. Quantifying channel development and sediment transfer following chute cutoff in a wandering gravel-bed river. Geomorphology 54(3-4), 307-323.

Galve, J.P., Gutiérrez, F., Lucha, P., Bonachea, J., Remondo, J., Cendrero, A., Gutiérrez, M., Gimeno, M.J., Pardo, G., Sánchez, J.A., 2009. Sinkholes in the salt-bearing evaporite karst of the Ebro River valley upstream of Zaragoza city (NE Spain): Geomorphological mapping and analysis as a basis for risk management. Geomorphology 108(3), 145-158.

Gay, G.R., Gay, H.H., Gay, W.H., Martinson, H.A., Meade, R.H., Moody, J.A., 1998. Evolution of cutoffs across meander necks in Powder River, Montana, USA. Earth Surface Processes and Landforms 23(7), 651-662.

Gökkaya, E., Gutiérrez, F., Ferk, M., Görüm, T., 2021. Sinkhole development in the Sivas gypsum karst, Turkey. Geomorphology 386, 107746.

Grenfell, M., Aalto, R., Nicholas, A., 2012. Chute channel dynamics in large, sand-bed meandering rivers. Earth Surface Processes and Landforms 37(3), 315-331.

Guerrero, J., Lucha, P., 2008. Impact of halite dissolution subsidence on Quaternary fluvial terrace development: Case study of the Huerva River, Ebro Basin, NE Spain. Geomorphology 100, 164-179.

Gustavson, T.C., 1986. Geomorphic development of the Canadian River Valley, Texas Panhandle: An example of regional salt dissolution and subsidence. GSA Bulletin 97(4), 459-472.

Gustavson, T.C., Simpkins, W.W., Alhades, A., Hoadley, A., 1982. Evaporite dissolution and development of karst features on the rolling plains of the Texas panhandle. Earth Surface Processes and Landforms 7(6), 545-563.

Gutiérrez, F., 1996. Gypsum karstification induced subsidence: effects on alluvial systems and derived geohazards (Calatayud Graben, Iberian Range, Spain). Geomorphology 16(4), 277-293.

Gutiérrez, F., Galve, J.P., Guerrero, J., Lucha, P., Cendrero, A., Remondo, J., Bonachea, J., Gutiérrez, M., Sánchez, J.A., 2007. The origin, typology, spatial distribution and detrimental effects of the sinkholes developed in the alluvial evaporite karst of the Ebro River valley downstream of Zaragoza city (NE Spain). Earth Surface Processes and Landforms 32(6), 912-928.

Gutiérrez, F., Parise, M., De Waele, J., Jourde, H., 2014. A review on natural and human-induced geohazards and impacts in karst. Earth-Science Reviews 138, 61-88.

Gutiérrez, F., Zarroca, M., Castañeda, C., Carbonel, D., Guerrero, J., Linares, R., Roqué, C., Lucha, P., 2017. Paleoflood records from sinkholes using an example from the Ebro River floodplain, northeastern Spain. Quaternary Research 88(1), 71-88.

Han, B., Endreny, T.A., 2014. Detailed river stage mapping and head gradient analysis during meander cutoff in a laboratory river. Water Resources Research 50(2), 1689-1703.

Harrison, L.R., Dunne, T., Fisher, G.B., 2015. Hydraulic and geomorphic processes in an overbank flood along a meandering, gravel-bed river: implications for chute formation. Earth Surface Processes and Landforms 40(9), 1239-1253.

Heritage, G.L., Milan, D.J., Large, A.R.G., Fuller, I.C., 2009. Influence of survey strategy and interpolation model on DEM quality. Geomorphology 112(3), 334-344.

Hooke, J.M., 1995. River channel adjustment to meander cutoffs on the River Bollin and River Dane, northwest England. Geomorphology 14(3), 235-253.

Hooke, J.M., 2007. Complexity, self-organisation and variation in behaviour in meandering rivers. Geomorphology 91(3-4), 236-258.

Howard, A.D., 1996. Modelling channel evolution and floodplain morphology. In: M.G. Anderson, D.E. Walling, P.D. Bates (Eds.), Floodplain Processes. John Wiley & Sons, Chichester, pp. 15-62.

Howard, A.D., 2009. How to make a meandering river. Proceedings of the National Academy of Sciences 106(41), 17245-17246.

Howard, A.D., Knutson, T.R., 1984. Sufficient conditions for river meandering: a simulation approach. Water Resources Research 20(11), 1659-1667.

Hyatt, J.A., Jacobs, P.M., 1996. Distribution and morphology of sinkholes triggered by flooding following Tropical Storm Alberto at Albany, Georgia, USA. Geomorphology 17, 305-316.

James, A.N., Cooper, A.H., Holliday, D.W., 1981. Solution of the gypsum cliff (Permian, middle Marl) by the River Ure at Ripon, North Yorkshire. Proceedings of the Yorkshire Geological Society 43(4), 433-450.

James, M.R., Robson, S., 2014. Mitigating systematic error in topographic models derived from UAV and ground-based image networks. Earth Surface Processes and Landforms 39(10), 1413-1420.

Johannesson, H., Parker, G., 1989. Linear theory of river meanders. In: S. Ikeda, G. Parker (Eds.), River meandering. Water Resources Monograph. AGU, Washington, pp. 181-214.

Johnson, R.H., Paynter, J., 1967. The Development of a Cutoff on the River Irk at Chadderton, Lancashire. Geography 52(1), 41-49.

Keller, E.A., Swanson, F.J., 1979. Effects of large organic material on channel form and fluvial processes. Earth surface processes 4(4), 361-380.

Lancaster, S.T., Bras, R.L., 2002. A simple model of river meandering and its comparison to natural channels. Hydrological Processes 16, 1-26.

Lane, S.N., Westaway, R.M., Hicks, D.M., 2003. Estimation of erosion and deposition volumes in a large, gravel-bed, braided river using synoptic remote sensing. Earth Surface Processes and Landforms 28(3), 249-271.

Lewis, G.W., Lewin, J., 1983. Alluvial Cutoffs in Wales and the Borderlands. In: J.D. Collinson, J. Lewin (Eds.), Modern and Ancient Fluvial Systems. Special Publications of the International Association of Sedimentologists. Wiley, pp. 145-154.

Luchi, R., Zolezzi, G., Tubino, M., 2011. Bend theory of river meanders with spatial width variations. Journal of Fluid Mechanics 681, 311-339.

McGowen, J.H., Garner, L.E., 1970. Physiographic features and stratification types of coarse-grained pointbars: modern and ancient examples. Sedimentology 14(1-2), 77-111.

Mertes, L., Dunne, T., Martinelli, L., 1996. Channel-Floodplain Geomorphology along the Solim??es-Amazon River, Brazil. Geological Society of America Bulletin 108, 1089-1107.

Micheli, E.R., Larsen, E.W., 2011. River channel cutoff dynamics, Sacramento River, California, USA. River Research and Applications 27(3), 328-344.

Milan, D.J., Heritage, G.L., Hetherington, D., 2007. Application of a 3D laser scanner in the assessment of erosion and deposition volumes and channel change in a proglacial river. Earth Surface Processes and Landforms 32(11), 1657-1674.

Milan, D.J., Heritage, G.L., Large, A.R.G., Fuller, I.C., 2011. Filtering spatial error from DEMs: Implications for morphological change estimation. Geomorphology 125, 160-171.

Morgan, S.E., Allen, D.M., Kirste, D., Salas, C.J., 2019. Investigating the hydraulic role of a large buried valley network on regional groundwater flow. Hydrogeology Journal 27, 2377-2397.

Morigi, A.N., James, J.W.C., 1984. The sand and gravel resources of the country north-east of Ripon, North Yorkshire, British Geological Survey, London.

Motta, D., Abad, J.D., Langendoen, E.J., Garcia, M.H., 2012. A simplified 2D model for meander migration with physically-based bank evolution. Geomorphology 163-164(0), 10-25.

NYCC, 2021. North Yorkshire County Council Historic Environment Record SMY No. MNY36263 Hutton Conyers WW1 Practice Range

NRFA, 2021a. National River Flow Archive: 27007 - Ure at Westwick. . UKCEH.

NRFA, 2021b. National River Flow Archive: 27086 - Skell at Ripon Alma Weir. UKCEH.

Parker, G., Shimizu, Y., Wilkerson, G.V., Eke, E.C., Abad, J.D., Lauer, J.W., Paola, C., Dietrich, W.E., Voller, V.R., 2011. A new framework for modeling the migration of meandering rivers. Earth Surface Processes and Landforms 36(1), 70-86.

Patterson, D.A., Davey, J.C., Cooper, A.H., Ferris, J.K., 1995. The investigation of dissolution subsidence incorporating microgravity geophysics at Ripon, Yorkshire. Quarterly Journal of Engineering Geology and Hydrogeology 28(1), 83-94.

Peakall, J., Ashworth, P., Best, J., 2007. Meander-Bend Evolution, Alluvial Architecture, and the Role of Cohesion in Sinuous River Channels: A Flume Study. Journal of Sedimentary Research 77, 197-212.

Powell, J.H., Cooper, A.H., Benfield, A.C., 1992. Geology of the Country Around Thirsk. Memoir for 1:50000 geological sheet 52 (England and Wales). H.M. Stationery Office, London.

Schwendel, A.C., Aalto, R., Nicholas, A., Parsons, D., 2018. Fill characteristics of abandoned channels and resulting stratigraphy of a mobile sand-bed river floodplain. In: M. Ghinassi, L. Colombera, N.P. Mountney, A.J.H. Reesink (Eds.), Fluvial Meanders and Their Sedimentary Products in the Rock Record, Int. Assoc. Sedimentologists, Special Publication 48. Wiley, Chichester, pp. 251-272.

Schwendel, A.C., Fuller, I.C., Death, R.G., 2012. Assessing DEM interpolation methods for effective representation of upland stream morphology for rapid appraisal of bed stability. River Research and Applications 28(5), 567-584.

Schwendel, A.C., Nicholas, A.P., Aalto, R.E., Sambrook Smith, G.H., Buckley, S., 2015. Interaction between meander dynamics and floodplain heterogeneity in a large tropical sand-bed river: the Rio Beni, Bolivian Amazon. Earth Surface Processes and Landforms 40(15), 2026-2040.

Sear, D., German, S., Hill, C.T., 2000. River Ure: Geomorphological Audit, Environment Agency, North East region.

Seminara, G., 2006. Meanders. Journal of Fluid Mechanics 554, 271-297.

Seyoum, W.M., Eckstein, Y., 2014. Hydraulic relationships between buried valley sediments of the glacial drift and adjacent bedrock formations in northeastern Ohio, USA. Hydrogeology Journal 22, 1193-1206.

Smith, C.E., 1998. Modeling high sinuosity meanders in a small flume. Geomorphology 25, 19-30.

Stolum, H.-H., 1996. River meandering as a self-organization process. Science 271, 1710-1713.

Sun, T., Meakin, P., Jossang, T., Schwarz, K., 1996. A simulation model for meandering rivers. Water Resources Research 32(9), 2937-2954.

Tal, M., Paola, C., 2010. Effects of vegetation on channel morphodynamics: results and insights from laboratory experiments. Earth Surface Processes and Landforms 35(9), 1014-1028.

Thompson, A., Hine, P.D., Greig, J.R., Peach, D.W., 1996. Assessment of subsidence arising from gypsum dissolution with particular reference to Ripon, Technical Report for the Department of the Environment, Symonds Travers Morgan, East Grinstead.

Thompson, D.M., 2003. A Geomorphic Explanation for a Meander Cutoff Following Channel Relocation of a Coarse-Bedded River. Environmental Management 31(3), 0385-0400.

Tooth, S., McCarthy, T.S., Brandt, D., Hancox, P.J., Morris, R., 2002. Geological controls on the formation of alluvial meanders and floodplain wetlands: the example of the Klip River, eastern Free State, South Africa. Earth Surface Processes and Landforms 27(8), 797-815.

Tunwell, D.C., Passmore, D.G., Harrison, S., 2016. Second World War bomb crater and the archaeology of Allied air attacks in the forests of the Normandie-Maine National Park, NW France. Journal of Field Archaeology 41(3), 313-330.

van Dijk, W.M., van de Lageweg, W.I., Kleinhans, M.G., 2013. Formation of a cohesive floodplain in a dynamic experimental meandering river. Earth Surface Processes and Landforms 38(13), 1550-1565.

Viero, D.P., Dubon, S.L., Lanzoni, S., 2018. Chute cutoffs in meandering rivers: formative mechanisms and hydrodynamic forcing. In: M. Ghinassi, L. Colombera, N.P. Mountney, A.J.H. Reesink (Eds.), Fluvial Meanders and Their Sedimentary Products in the Rock Record, Int. Assoc. Sedimentologists, Special Publication 48. Wiley, Chichester, pp. 201-230.

Virtanen, P., Gommers, R., Oliphant, T.E., Haberland, M., Reddy, T., Cournapeau, D., Burovski, E., Peterson, P., Weckesser, W., Bright, J., van der Walt, S., Brett, M., Wilson, J., Millman, K.J., Mayorov, N., Nelson, A.R.J., Jones, E., Kern, R., Larson, E., Carey, C.J., Polat, I., Feng, Y., Moore, E.W., VanderPlas, J., Laxalde, D., Perktold, J., Cimrman, R., Henriksen, I., Quintero, E.A., Harris, C.R., Archibald, A.M., Ribeiro, A.H., Pedregosa, F., van Mulbregt, P., Contributors, S., 2020. SciPy 1.0: Fundamental Algorithms for Scientific Computing in Python. Nature Methods 17, 261-272.

Waltham, A.C., Bell, F.G., Culshaw, M.G., 2005. Sinkholes and Subsidence; Karst and cavernous rocks in engineering and construction. Praxis, Springer, Chichester, UK.

Woodget, A.S., Carbonneau, P.E., Visser, F., Maddock, I.P., 2015. Quantifying submerged fluvial topography using hyperspatial resolution UAS imagery and structure from motion photogrammetry. Earth Surface Processes and Landforms 40(1), 47-64.

Zinger, J.A., Rhoads, B.L., Best, J.L., 2011. Extreme sediment pulses generated by bend cutoffs along a large meandering river. Nature Geoscience 4(10), 675-678.

Zolezzi, G., Luchi, R., Tubino, M., 2012. Modeling morphodynamic processes in meandering rivers with spatial width variations. Reviews of Geophysics 50, RG4005.

Supplementary materials:

S1: Video footage of flood discharge via the chute channel on 27th September at sinkhole groups G7 and G8 while the majority of the flow was still routed around the meander bend. Video courtesy of David Powell (Yorkshire Wildlife Trust). File: 20190927_120519.mp4

S2: Aerial video of the initial chute channel taken in late October at low flow showing coalescence of sinkholes and thresholds between them, gravel and cobble exposures in the sinkhole sides, deposition of coarse sediment at their lower ends and the configuration of the river bend upstream with the main flow directed past the chute entrance across a dissected point bar. The flight path starts and sinkhole group G6, moving over G5 and G2 with G3 visible on the right towards the upper end of the chute channel (sinkholes groups are defined in Fig. 8). Video courtesy of Chris Osborne (Yorkshire Wildlife Trust). File: Ripon Loop UAV - credit Chris Osborne (3).MP4